JOINT EUROPEAN TORUS JET

JET–P(88)44

J.A. Wesson, R.D. Gill, M. Hugon, F.C. Schüller, J.A. Snipes, D.J. Ward, D. Bartlett, D.J. Campbell, P.A. Dupperex, A.W. Edwards, R.S. Granetz, N.A.O. Gottardi, T.C. Hender, E. Lazzaro, P.J. Lanas, N. Lopes-Cardozo, F.K. Mast, M.F.F. Nave, N.A. Salmon, P. Smeulders, P. Thanas, B. Tubbing, M.F. Turner, A. Weller and JET Team

Disruptions in JET

Disruptions in JET

J.A. Wesson, R.D. Gill, M. Hugon, F.C. Schüller, J.A. Snipes, D.J. Ward, D. Bartlett, D.J. Campbell, P.A. Dupperex, A.W. Edwards, R.S. Granetz, N.A.O. Gottardi, T.C. Hender[1], E. Lazzaro, P.J. Lanas, N. Lopes-Cardozo, F.K. Mast, M.F.F. Nave, N.A. Salmon, P. Smeulders, P. Thanas, B. Tubbing, M.F. Turner[1], A. Weller and JET Team*

JET-Joint Undertaking, Culham Science Centre, OX14 3DB, Abingdon, UK

[1]UKAEA/EURATOM Fusion Association. Culharm Laboratory, OX14 3DB, Abingdon, Oxon, UK
** See annex of P.Lallia et al, "Plasma Heating in JET",*
(13th EPS Conference on Controlled Fusion and Plasma Physics, Schliersee, Germany (1986)).

Preprint of Paper to be submitted for publication in
Nuclear Fusion

ABSTRACT

In JET both high density and low-q operation are limited by disruptions. The density limit disruptions are caused initially by impurity radiation. This causes a contraction of the plasma temperature profile and leads to an mhd unstable configuration. There is evidence of magnetic island formation resulting in minor disruptions. After several minor disruptions a major disruption with a rapid energy quench occurs. This event takes place in two stages. In the first there is a loss of energy from the central region and in the second there is a more rapid fall to a very low temperature, apparently due to a dramatic increase in impurity radiation. The final current decay takes place in the resulting cold plasma.

During the growth of the mhd instability the initially rotating mode is brought to rest. This mode locking is believed to be due to an electromagnetic interaction with the vacuum vessel and external magnetic field asymmetries.

The low-q disruptions are remarkable for the precision with which they occur at $q_\psi=2$. These disruptions do not have extended precursors and minor

disruptions. The instability grows and locks rapidly. The energy quench and current decay are generally similar to those of the density limit disruption.

INTRODUCTION

The earliest tokamak experiments exhibited major disruptions which terminated the plasma discharge and these have been observed in all subsequent tokamaks [1]. Detailed experimental studies of disruptions have been made in many machines [2-7] and the operating conditions leading to disruption have also been investigated [eg. 8,9]. Many theoretical attempts have been made both to identify the underlying causes of the disruption, such as the role of radiation loss in the energy balance [10], and to explain the mhd processes involved in the disruption [1,3]. In particular, the important role of growing m=2 island has long been recognised [eg. 11,12]. However, the subject remains poorly understood and therefore detailed studies of the occurrence and behaviour of disruptions in JET have been made both to determine the constraints which they impose on operation of the machine and to attempt to understand the underlying physics, as has been partially reported elsewhere [13-19]. The subject is complicated, firstly because disruptions can be caused in different ways and secondly because they involve a complex sequence of events.

The central characterising feature of disruptions is the sudden deterioration of the plasma. In JET the plasma energy can be lost in a few hundred microseconds. The event is almost always irreversible and the much increased resistance of the plasma leads to a rapid decay of the plasma current.

There are two principal categories of disruptions, defined by the operational limitation they impose. These are the density limit disruptions and the low-q disruptions. The larger part of this paper is devoted to

density limit disruptions, mainly because these disruptions are more complex, involving a sequence of many events.

In density limit disruptions it is found that at a given plasma current there is a limit to the plasma density which can be achieved without a disruption occurring. In JET this limit is due to the increase in impurity radiation with increasing density. The radiated power increases to a level where it equals the power input. This causes a contraction of the temperature profile and leads to the development of an mhd unstable current distribution. The ensuing instabilities result in a rapid energy loss. This is accompanied by a sudden increase in the plasma resistance producing a fast decay of the plasma current. As will be seen later, the final stage is quite complex and is not fully understood. Another common feature of density limit disruptions is the occurrence of several minor disruptions, from which the plasma recovers, before the final major disruption brings what is usually an irreversible change in the plasma.

Low-q disruptions are simpler in that they do not involve a long sequence of precursor behaviour. When the current is raised to a point at which q reaches a critical value there is a rapid growth of mhd instability followed immediately by an energy loss and current decay similar to that of the final phase of a density limit disruption.

A further type of disruption occurs during the current rise. These disruptions depend upon the details of the plasma formation during the current rise and are therefore also complicated.

Some unity can be introduced into the subject by recognising that for each type of disruption a central characteristic appears to be the production of a strong mhd instability. In the case of density limit and low q disruptions this appears to be brought about by a current profile which is strongly unstable to the m=2 mode. The requirement for a strong instability is that a steep current gradient should lie close to and inside

the resonant q=2 surface. In the case of the density limit disruptions this occurs through the contraction of the current profile to bring a strongly destabilising current gradient inside the q=2 surface and in the low-q disruptions the increase in current moves the q=2 surface outward to the edge of the plasma, again placing it in a strongly destabilising position in relation to the current gradient.

We shall now briefly summarise the results under headings which will then be used in the body of the paper.

Operational Overview

The density and low-q limit are described in the context of the Hugill diagram which plots disruptions in the $(1/q_a, \bar{n}R/B_\phi)$ plane where q_a is the safety factor at the edge of the plasma, $\bar{n}$ is the average electron density, R is the major radius of the plasma (= 3m in JET) and B_ϕ is the toroidal magnetic field. The disruption boundary for ohmically heated plasmas is given approximately by:

density limit $\quad \bar{n} = 12\times10^{19} B_\phi/Rq_c \quad (m^{-3})$

low-q limit $\quad q_\psi = 2$

where q_c is the cylindrical approximation for q defined by $q_c = 2\pi abB_\phi/\mu_o RI$, a and b being the half-width and half-height of the plasma and I the plasma current, and q_ψ is the actual value of q at the plasma edge. The density limit is increased with the application of additional heating.

Density Limit Disruptions

The events which constitute the complete disruption can be placed in the following sequence.

1) Radiative contraction

As the density is increased the power radiated from impurities also increases. When this power is approximately equal to the input power the temperature profile starts to contract. This can be understood in terms of an instability of the energy balance in which the heating of the plasma is unable to sustain the level of radiative power and the radiation then takes place at the expense of the internal energy of the plasma.

In principle the contraction could lead to a new equilibrium with a narrower current channel but in practice the plasma becomes mhd unstable before this equilibrium is reached.

2) Precursor instabilities

While the radiative contraction is taking place, mhd instabilities appear, principally m=2, n=1. This instability rotates with a frequency typically $\sim$500 Hz. When the magnitude of perturbation of the poloidal magnetic field reaches a value $\sim$10 gauss the mode is brought to rest and subsequently a minor disruption occurs. The mhd instability is identified as a tearing mode from the observed behaviour of the electron temperature around the q=2 surface. A flattening of the temperature is observed consistent with the magnetic island expected from the instability.

The minor disruption consists of a rapid radial redistribution of the plasma energy as diagnosed by the ECE temperature measurements. The plasma recovers from this event and the temperature profile moves towards its earlier form. However, this is halted by another minor disruption and a sequence of minor disruptions then takes place. This sequence finally ends in a major disruption. The behaviour of the minor disruptions is consistent with a model in which the temperature and current profiles relax through the growth of a magnetic island.

3) Energy quench

The major disruption is characterised by a sudden loss of the plasma energy. The first sign of this is seen on both the soft X-rays and the ECE. A loss of emission takes place in the core of the plasma on a timescale $\sim$1 ms. This loss has an m=1 structure similar to that reported by Tsuji et al [6], but does not appear to be an m=1 internal instability of the sawtooth type. It is followed after a time $\sim$1 ms by an even more rapid drop in the electron temperature on a timescale $\sim$50 μs. Virtually all of the plasma energy is lost at this time and the temperature does not recover.

The behaviour in this phase is not understood but does not appear to be explained simply by the widely accepted model of a high thermal conductivity resulting from resistive mhd turbulence.

4) Current decay

The energy quench phase of the disruption leaves the plasma in a highly resistive state, the plasma resistance typically being increased by a factor 10^2-10^3 over its normal value. The reason for this is the very low temperature which may be as low as $\sim$10 eV. Since the current is initially hardly affected, the ohmic heating, I^2R_η, is also enormously increased resulting in input powers of the order of a gigawatt, this power coming from the decay of the poloidal magnetic field energy. The picture is completed and made consistent by the fact that the input power is balanced by an equal impurity radiation power and the electron temperature is trapped at a low value by this radiation.

There are also two interesting types of behaviour where the plasma resistance falls back to a small value. In one set this is just due to a recovery of the plasma temperature and a fall in the radiation. In the other the plasma current is transferred to runaway electrons.

Apart from the intrinsic interest of the physics of the current decay it also has operational significance in that, depending on the resistance of the plasma as compared with that of the vacuum vessel, a substantial part of the plasma current can be transferred to the vacuum vessel leading to forces of hundreds of tonnes.

Low-q Disruptions

To study the low-q disruption boundary, experiments were carried out with a toroidal field of 1.7 T. In each shot the current was increased until a disruption occurred and this was done for densities in the range $2\text{-}6\times10^{19}m^{-3}$. The disruptions occurred in a narrow range of the "topological" q value, $q_\psi = 2\pm0.1$. The corresponding cylindrical q values are around 1.5. The plasma current was 3.5 MA and a disruption boundary at $q_\psi = 2$ would correspond to a current of 7 MA at the full toroidal field, $B_\phi = 3.4$ T.

The low-q disruptions are sudden, with only a short time, $\sim$10 ms, between the mode lock and the hard disruption. There is no radiation induced contraction and there are no precursor oscillations or minor disruptions.

At high density these low-q plasmas give the highest value of the Murakami parameter achieved on JET, $\bar{n}R/B_\phi = 7.2\times10^{19}m^{-2}T^{-1}$.

Current Rise Disruptions

Density limit disruptions occurring during the current rise phase of JET discharges can be recognised by the high radiated power and high values of internal inductance. However, of specific interest here are disruptions associated with hollow or fairly flat current profiles which are characteristic of the current rise phase, particularly at low density. In

order to avoid such disruptions the rate of rise of plasma current has to be kept small. Typically, in the final stages of a current ramp to 5 MA, dI/dt must be less than 0.5 MA/sec if instability is to be avoided.

Vertical Instability Disruptions

Because of the elongated plasma in JET, the axisymmetric (n=0) instability has to be controlled by feedback. Failure of this control leads to a vertically unstable displacement of the plasma. This is not in itself a disruption but can lead to a disruption through the reduction of the surface value of q.

Diagnostics

JET has a wide range of diagnostics but for the present work most use has been made from data taken by the magnetic diagnostics, the bolometry, the ECE systems and the soft X-ray cameras. Figure 1 shows the location of some of these systems on a plan of the JET torus. The magnetic diagnostics include arrays of 18 tangential B_θ field pick-up coils and 14 normal field saddle loops situated around the poloidal cross-section on each octant (figure 2). Magnetic coil combinations provide n=1,2 and 3 tangential field signals (B_θ) and n=1 and 2 radial field signals (B_r). Sampling rates are usually 200 μs but have been reduced to 25 μs in some cases. The magnetic diagnostic signals were also used to produce a trigger signal when a disruption was detected and this was used to initiate data collection on several other diagnostics at high sampling rates.

The total radiated power is determined from inversion of data from bolometer cameras which have 14 vertical and 20 horizontal lines of sight [20]. The system has a time resolution of 20 ms.

Several ECE systems are used (figure 3) including a Michelson interferometer [21], a polychromator [22] and a heterodyne radiometer [23],

all located at the same toroidal position in octant 7. The Michelson measures complete profiles at low time resolution; the other instruments can resolve smaller time intervals (down to 25 μs) and measure T_e with high accuracy over a restricted radial extent in and just above the horizontal midplane. The polychromator has a radial resolution of 6 cm and a transverse resolution of 7 cm. The radiometer has the same transverse resolution and resolution of 1.5 cms radially. The viewing lines are shown in figure 3.

Vertical and horizontal X-ray cameras [24] containing 100 detectors (figure 4) measure the X-ray emission along a line of sight with spatial resolution of 7 cm and time resolution of approximately 5 μs in a single poloidal plane in octant 2; the toroidal variations in X-ray emission are measured by 5 cameras each with 4 detectors mounted at different positions around the machine.

I. OPERATIONAL OVERVIEW

To give some pattern to the study of disruptions it is common to use the Hugill diagram in which the boundaries imposed on operations by the occurrence of disruptions are plotted in the $(1/q_c, \bar{n}R/B_\phi)$ plane.

Figure 5 shows two sets of results in the Hugill diagram. Figure 5(a) gives points for a set of disruption free discharges in which parameter scans were carried out for transport analysis. Figure 5(b) gives points for discharges which <u>did</u> disrupt. It is clear from these figures that the position in the $(1/q_c, \bar{n}R/B_\phi)$ does not by itself determine whether a discharge will or will not disrupt. On the other hand the figures show clearly the limitation of operation which is imposed by disruptions at high $\bar{n}$ or low q_c.

Factors other than q_c and nR/B_ϕ which are found to play a determining

role are: i) the level of impurity as indicated by the effective ionic charge Z_{eff}, ii) the use of additional heating, which increases the achievable density, iii) the preceding form of dI/dt and iv) the use of injected pellets.

The operational aspects can be seen from another point of view using a different diagram which uses the parameters q_ψ and the dimensionless internal inductance ℓ_i, defined by

$$\ell_i = \frac{2}{\mu_o^2 R I^2} \int B_\theta^2 d\tau$$

where the integral is taken over the plasma volume.

In this space q_ψ is a directly controllable parameter but ℓ_i is only partly subject to control. Figure 6 shows the operation space in this diagram together with the types of instability and disruption which occur in different regions along the boundary.

When we later look at the physics of the density limit disruption it will be seen that the disruption process is initiated when 100% of the input power is lost by impurity radiation. This balance is dependent on a complicated mixture of atomic and transport processes. It cannot be expected therefore that a simple boundary in the Hugill diagram can be derived. However the basic features can be brought out as follows.

The radiated power P_r has the dependence

$$P_r \propto n_r^2 \, f \, R \, A$$

where n_r is the electron density characterising the radiating region, normally at the plasma edge, f is the fractional impurity concentration and A is the area of plasma involved.

With ohmic heating the input power is given by I^2R_η where R_η is the plasma resistance. However R_η depends upon the plasma temperature and this in turn depends upon the confinement time, τ_E. Thus, rather than introduce an empirical scaling law for τ_E, it is simpler to use the scaling law for ohmic power. On JET this is found to have the approximate dependence

$$P_\Omega \propto \frac{B_\phi b}{R\, q_c^{1.5}}$$

where b is the half-height of the plasma. Thus the condition $P_r = P_\Omega$ takes the form

$$\frac{n_r^2\, R^2}{B_\phi} = \text{const.x}\, \frac{1}{q_c^{1.5}}\, \left(\frac{b}{Af}\right).$$

This relation shows how the parameters of the Hugill diagram arise, together with the uncertainties and imperfections of this description. The f dependence can be replaced approximately by $Z_{eff} - 1$ where Z_{eff} is the effective ion charge in the plasma.

With a substantial additional heating power, P_{add}, the above model would give a critical density

$$n_r \propto P_{add}^{\frac{1}{2}}.$$

This improvement is found to hold for neutral beam heated plasmas. With ICRH the improvement is somewhat less and this can be explained by the observed increase in Z_{eff}.

The low-q disruption boundary was explored in experiments with

B_ϕ = 1.7T, R = 2.97m, a = 1.2m and b/a = 1.35. Figure 7 gives the time trajectories of the discharges in the $(1/q_\psi, \bar{n}R/B_\phi)$ plane. It is seen that the disruptions occur very close to $q_\psi = 2$, the corresponding value of q_c being 1.5. The highest value of the Murakami parameter for JET was achieved under these conditions in a non-disruptive discharge with $\bar{n}R/B_\phi = 7.2 \times 10^{19} m^{-2} T^{-1}$ and with $q_\psi = 2.2$. The plasmas with q_ψ just above 2.0 were quite reproducible. The sawtooth inversion radius of these discharges was 55% of the minor radius.

Disruptions are also caused by too high a rate of current rise for the chosen density evolution. These are preceded by a sequence of mhd instabilities initially having mode numbers $m = q_\psi$. The final mode number can be either m = 3 or m = 2. The critical current ramp-rate above which particular care is needed is $\dot{I}$ = 0.7MA/s. Ramp-rates above 1MA/s are very difficult to achieve except during the early low temperature phase. The operational implication of these disruptions arises from the requirement of a rapid current rise for high current (> 5MA) discharges because of the volt-second limitation.

Another situation which can cause disruption is brought about by the n = 0, axisymmetric instability. This mode is normally controlled by feedback. However if this control is lost an unstable vertical displacement takes place. The top or bottom of the vessel then acts as a limiter. The effective value of q_ψ falls and a disruption follows at $q_\psi = 2$. The inverse phenomenon can also occur, a disruption leading to increased elongation and a loss of feedback control of the vertical instability.

The energy quench produces a substantial force on the vacuum vessel. The loss of plasma pressure leads to an increase in the toroidal magnetic field pressure inside the plasma $\delta(B_\phi^2/2\mu_o) \sim \delta p$ and from flux conservation

this lowers the toroidal magnetic field between the plasma and the vacuum vessel. The current induced in the vacuum vessel is such that the inward pressure on the vacuum vessel is approximately equal to the volume average of the change in plasma pressure, $\bar{\delta}p$. This is typically of the order of a few tonnes/m². The current decay which follows the energy quench also produces a rearrangement of the toroidal magnetic field and a fast decay leads to an outward pressure in the vacuum vessel of approximately $B_{\theta v}^2/2\mu_o$, where $B_{\theta v}$ is the initial poloidal magnetic field at the vacuum vessel. For a 5 MA plasma this pressure is of the order of 10 tonnes/m².

A further force on the vacuum vessel arises during the current decay. The inductive voltage from the plasma current decay drives a current in the vacuum vessel $I_v \sim (L_v/R_v)\,\dot{I}$ where L_v is the effective inductance of the vacuum vessel and R_v is its toroidal resistance, and I is the plasma current. This leads to a pressure on the vessel

$$p_v \sim \frac{B_{\theta v}^2}{\mu_o} \frac{\tau_{vessel}}{\tau_{decay}}$$

where $\tau_{vessel} = L_v/R_v$ and τ_{decay} is the plasma current decay time. Since τ_{vessel} = 4ms, a disruption with τ_{decay} = 10ms in a 5MA plasma leads to a pressure of ~10 tonnes/m².

Figure 8 gives the dependence of the current decay rate on the value of the current at the start of the decay. For slow current decay times, typically 250ms, the radial position control amplifier has enough voltage capability to reduce the vertical field sufficiently fast to hold the plasma in the required position. For faster decay rates the position control amplifier saturates, leading to a vertical field which is too large to hold the plasma in position. The result is that the plasma is driven on to the

inner wall. The decay time can be as short as 10ms and the highest value of dI/dt is around 900MA/s.

II. DENSITY LIMIT DISRUPTIONS

The sequence of events in density limit disruptions is rather complex. Before presenting the detailed results therefore, we give for orientation a simple figure showing several of the diagnostic measurements during the whole current pulse.

Thus figure 9 shows a disruption from a flat top current of 3.0MA induced by an imposed increase in the electron density. It is seen that the density increase causes an increase in radiated power. The radiated power increases until it equals the input ohmic power and shortly afterwards pre-disruption behaviour is seen on all diagnostics. The causal link is the contraction of the plasma caused by the radiation, leading to mhd instability. Both the density and the electron temperature fall during this pre-disruption phase of $\sim$ 1s. The contraction of the plasma is recorded by the drop in both the edge bolometer and H_α signals but the subsequent pulses of H_α indicate irregular interaction with the limiter. This irregular behaviour is also seen on the voltage loop and the radiated power. The final, rapid temperature fall signals the energy quench. This is then followed by the rapid current decay and its associated large loop voltage together with an enormous (off-scale) radiated power from impurities in the now very low temperature plasma.

We shall now describe the density disruptions under the headings of the four basic phases - radiative contraction, precursor instabilities, energy quench and current decay phase.

1) Radiative Contraction

The possibility that impurity radiation could set a limit to the achievable density in a tokamak has been discussed theoretically in several papers [10,25-31]. The basic idea is that increasing the electron density increases the radiation loss and at some point a radiation contraction occurs leading to a disruption. The evidence from JET confirms this model.

i) Radiation behaviour

Since the disruption is driven by radiation it is important to study the radial and poloidal evolution of the radiated power and understand how it leads to an unstable configuration. The experimental behaviour on JET has three main phases:

a) Before 100% radiation is reached, most of the radiated power comes from a region poloidally localised near the limiter where particle recycling leads to enhanced impurity line radiation.

b) Immediately following 100% radiation, a marfe [32] occurs. This is a toroidally symmetric but poloidally localised region of dense, cold plasma near the plasma edge which radiates more strongly than the rest of the plasma. The marfe is normally situated on the small major radius side of the torus, away from the limiter and accompanies a rapid increase in radiated power.

c) After 50-100ms, the marfe decays and the radiation then comes from a poloidally symmetric ring around the plasma edge. The temperature profile shrinks away from the limiter.

Figure 10 shows the time evolution of the radiated power fraction around the time at which 100% radiation is reached and indicates the three phases described above. The radiation increase was due to a steady rise in electron density and the discharge terminated in a disruption 1.5s later. Figure 11 shows the

profiles of radiated power density across the horizontal mid-plane before and after 100% radiation is reached at the times indicated in figure 10. This shows the asymmetry of the initial radiation profile.

Asymmetry of the radiation profile is due initially to interaction with the limiter. As the density rises there is an increase in radiated power and a decrease in edge temperature, with a corresponding decrease in parallel thermal conductivity. The plasma becomes unstable to a marfe which, being localised in poloidal angle, can only be unstable when the parallel thermal conductivity at the edge becomes small. The marfe accelerates the increase in radiated power and the drop in edge temperature, the process continuing until the plasma is again stable to marfes. At the same time the limiter interaction decreases since all the input power is being radiated. Finally, with no marfe and no limiter interaction, the radiation profile is nearly symmetric.

ii) Contraction of the temperature profile

Having reached 100% radiation, the next step in a density limit discharge is for the temperature and radiation profiles to contract away from the limiter. This is seen in figure 12 where the temperature and radiation profiles are shown at three times during a contraction.

It is expected that when 100% of the input power is radiated, the edge temperature gradient should go to zero since no heat is being conducted out of the edge plasma. This applies whether the power is radiated from the edge of the plasma or from the centre. What is not clear, however, is under what conditions the temperature profile should contract inwards on an energy confinement timescale as is observed. In fact, a simple analysis shows that the plasma can be either stable or

unstable to radiation contraction, depending predominantly on the density profile and how it changes as the temperature profile contracts.

The physics involved in the contraction is complex but the behaviour of a simple model [14] gives insight into the experimental behaviour. Assuming the plasma to be cylindrical with the radiation coming from a thin shell, the power balance equation may be written

$$\frac{d}{dt}\,\epsilon(a_p) = I^2\rho(a_p) - Cn^2 a_p \delta - \frac{KT_o}{a-a_p}\,a_p \qquad (1)$$

where a_p is the radius of the radiation maximum, ϵ the average plasma energy per unit length, ρ the plasma resistance per unit length, C is a constant, K the thermal conductivity, δ the width of the radiating layer and T_o is the temperature at which the radiation peaks. The first term on the right hand side represents the input power, the second term, the radiated power and the third, the power conducted out of the plasma edge. In equilibrium these are in the ratio $1:\phi:(1-\phi)$, where ϕ is the radiated power fraction.

Linearising Eq.(1) at constant current and assuming for simplicity that δ remains constant yields the stability equation

$$\frac{a_p}{\epsilon}\frac{d\epsilon}{da_p}\,\gamma\tau_E = \left(\frac{a_p}{\rho}\frac{d\rho}{da_p} - \phi\left(1 + \frac{2a_p}{n}\frac{dn}{da_p}\right) - (1-\phi)^2\,\frac{a}{a-a_p}\right) \qquad (2)$$

where γ is the growth rate of a perturbation to a_p. Stability to contraction is determined by the sign of γ and, in this simplified analysis, stability depends on the changes in the plasma resistance and the electron density in the radiating layer, as the plasma contracts.

These depend on transport processes which are not well understood but the behaviour of the model under simple assumptions is easily investigated, giving insight into the experimental behaviour.

Assuming that the density profile remains fixed as the temperature profile contracts and that the plasma resistance is proportional to $\frac{1}{a_p^2}$, a stability criterion can be derived. Substituting for $(a-a_p)$ in terms of the power conducted out of the plasma, yields the condition for instability

$$-\frac{a}{n}\frac{dn}{dr} > \frac{1}{2} - \frac{a}{2\rho}\frac{d\rho}{dr} + (1-\phi)^2 \frac{I^2\rho}{2KT_o}.$$

where the experimental observation that the stored energy decreases during contraction has been used.

For a JET plasma with I = 3MA, loop voltage 1V, major radius 3m, and assuming $K = 3\times10^{19}m^{-1}s^{-1}$ and T_o = 100eV, the gradient $\frac{a}{n}\frac{dn}{dr} \sim 10$ from figure 13 gives instability for

$$\phi \gtrsim 0.9.$$

The stability to contraction at substantially less than 100% radiated power arises because the radiating layer is assumed to occur at a low temperature, representative of low Z impurity line radiation. As long as a substantial fraction of the input power is conducted out of the plasma edge, the temperature gradient must remain large and hence the radiation layer is close to the edge. Eq.(2) is dominated by the last term as long as $a-a_p$ is small and $\phi \ll 1$. As ϕ approaches unity this term becomes small and instability is possible.

The requirement that ϕ must approach unity for instability to occur can be removed if the logarithmic density gradient, the driving term for the instability, is assumed to be singular at $a_p = a$ [33]. However, this is clearly not the case for a typical density profile.

The model predicts two types of behaviour which could be observed as a radiation contraction in tokamaks.

a) The plasma remains in thermal contact with the limiter until 100% of the input power is radiated. If $\frac{a}{n}\frac{dn}{dr}$ is sufficiently small the plasma is stable to the instability described above. Increasing the radiation further (by increasing the density for instance) will lead to a <u>stable</u> contraction of the temperature profile on the timescale of the density increase. This contraction could be stopped by stopping the density increase.

b) On reaching 100% radiation the density gradient at the edge is steep, the plasma is <u>unstable</u> to a contraction of the temperature profile on the energy confinement timescale. This contraction continues until a new equilibrium is reached with a smaller cross-section, even if the density is not increased further. The simple model predicts the edge density gradient required for instability

$$-\frac{a}{n}\frac{dn}{dr} \gtrsim \frac{3}{2}$$

compared with a value $\sim$ 10 on JET. This predicts that JET should behave according to b) above, and this is consistent with observation.

iii) Evolution to an mhd unstable equilibrium

The contraction of the temperature profile, once 100% radiation is reached, generally leads to plasma instabilities, rather than just an equilibrium plasma with a smaller cross-section. Preceding a density limit disruption there is a period of the order of 1 second between reaching 100% radiation and the final loss of energy. During this time, magnetic perturbations are observed at the plasma edge with corresponding perturbations observed in ECE and soft X-ray measurements. The way in which a contraction of the temperature profile and narrowing of the current channel leads to an unstable configuration has been discussed previously and is outlined below.

It is generally observed that the m=2 tearing mode plays an important role in disruptions, so the change in stability of this mode during a contraction of the temperature profile is considered. The energy available to drive this mode can be written [12]

$$\delta E = \frac{\pi^2 R}{2} \int \frac{dj/dr}{(2-q)B_\theta} B_r^2 r^3 dr,$$

where the integral is evaluated over the regions outside the island. A negative value for δE implies destabilisation. A negative current gradient destabilises the mode in a region where $q < 2$ and has a stabilising effect in a region where $q > 2$. During contraction of the temperature profile, the current channel narrows and current gradients increase, affecting the stability of the mode.

To illustrate this behaviour, the contraction has been modelled using a 1-D code which follows energy transport, resistive diffusion of current and the quasi-linear growth of tearing modes [34]. The effect of sawtooth activity in the core is included. Figure 14 shows the

calculated temperature profiles before and after contraction for a plasma with q(a) = 5. The flattening around r = 0.85 m after contraction is the effect of an m=2 magnetic island which has grown as a result of the current gradient steepening within q=2. During this contraction, the simulation produced a change in internal inductance, ℓ_i, of ∿ 15%. The experimentally inferred value under similar conditions changes by ∿ 12% between reaching 100% radiation and the growth of an m=2 mode. In both the experiment and the calculation, the contraction of the radiation layer from the edge to the q=2 surface proceeds on a timescale of ∿ 0.5s.

The effect of radiation on energy balance, the contraction of the temperature profile and the subsequent evolution to an MHD unstable equilibrium are apparently understood. On increasing the radiated power, the plasma can become unstable to a contraction of the temperature profile. The associated narrowing of the current channel increases current density gradients and drives mhd instabilities.

2. Precursor Phase

i) Magnetic perturbations

Shortly after the start of the radiation contraction, growing magnetic oscillations are observed on the magnetic coils and saddle loops around the plasma. The magnetic coils measure the rate of change of the poloidal magnetic field and the saddle loops measure the rate of change of the normal magnetic field (figure 2).

The observed magnetic oscillations have low poloidal and toroidal mode numbers (m and n) and appear to be due to the non-linear tearing modes which are predicted for typical current profiles. The magnetic perturbations are then associated with magnetic islands at the

corresponding rational magnetic surfaces. The magnetic field oscillates because the islands are rotating. At a later stage in the growth of the magnetic perturbation the magnetic islands stop rotating, becoming locked in position, and the subsequent growth in the magnetic field occurs without oscillation.

Figure 15 illustrates the simplest type of behaviour for a shot with B_ϕ = 2T, I = 2MA, R = 3.04m, a = 1.16m, elongation of 1.43 and, at the plasma edge, q_ψ = 4.95, q_c = 3.4. The $\dot{B}_\theta$ signal shows several bursts of small amplitude m=2 oscillations (10.63s - 10.73s) before undergoing a stronger growth which leads to locking. The amplitude of the perturbed poloidal field $\tilde{B}_\theta$ at the time of locking (10.768s) is 7G. The subsequent growth is measured using the saddle loops which are connected to measure the n = 1 perturbed radial magnetic field, $\tilde{B}_r$ [35]. It is seen from the figure that this grows almost linearly until the major disruption ($\sim$ 10.84s) and the onset of the current decay. The magnitude of the magnetic perturbation $\tilde{B}_r$ at this time is 40G.

Figure 15 also shows an expanded trace of the $\dot{B}_\theta$ signal. The initial frequency is 1.2kHz. The frequency then falls over a time of 20 ms before locking occurs. This is thought to be due to a change in velocity of the plasma which continues until the magnetic islands are brought to rest, the force being due to an electromagnetic interaction with the vacuum vessel. The physics of this process will be outlined later.

The simple behaviour shown in figure 15 is not the general type. Often the behaviour is more like that given in figure 16 where the magnetic activity lasts much longer and is more complex. (This shot, 11051, which will be analysed in more detail later, has B_ϕ = 3.4T, I =

2MA, R = 3m, a = 1.17m, an elongation ratio 1.3, and at the plasma edge q_ψ = 7.3 with q_c = 5.3.) It is seen that a burst of magnetic oscillations precedes the mode locking measured on the $\tilde{B}_r$ (n=1) signal at 7.89s. After this time a series of soft disruptions occurs with recurrence times of 100-200 ms. These are indicated on the $\tilde{B}_r$ (n=1) signal by short periods of rapid growth. Finally at 9.25s the final major disruption occurs.

It should be noted that after the initial locking at 7.89 seconds there is a brief unlocking as indicated in figure 16 by the removal of the locked $\tilde{B}_r$ (n=1) signal between 8.02s and 8.07s together with the burst of $\dot{B}_\theta$ oscillations preceding the second locking at 8.07s. It is seen that the first locking is associated with an m=3, n=1 perturbation while the second is associated with m=2, n=1. It is of interest to note that n=2 oscillations are seen ($\sim$ 7.97s) even when the m=3, n=1 mode is locked showing that islands on different magnetic surfaces are moving at different velocities.

ii) Electron temperature behaviour

We now turn to the effect of the magnetic perturbations on the electron temperature. The measurements were made with an 8 channel high resolution heterodyne radiometer.

Figure 17 shows the time dependence of the temperature at 8 radial locations. Three bursts of oscillation are indicated by arrows. Comparison with figure 16 indicates that the first burst (A) has m=3, n=1 and m≥4, n=2 components, the second (B) has m=5, n=2 and the third (C) m=2, n=1 and m=4, n=2 components. The surfaces which would be associated with these mode numbers have q=3, 2.5 and 2. The locations of these surfaces as determined from an equilibrium code based on the

magnetic measurements are R=3.93, 3.85 and 3.75m in the mid-plane. The locations of the observed electron temperature oscillations are close to the radii R=3.89, 3.85 and 3.78m indicating that these bursts of oscillation are associated with the corresponding rational surfaces.

The lower part of figure 17 shows an expanded trace of these temperature oscillations. The position of the q=2 surface is calculated (to ± 0.1m) from an equilibrium reconstruction and is found to lie in the region of maximum oscillation. These oscillations are therefore taken to be associated with this surface. The oscillations are non-sinusoidal indicating non-linear effects, which corroborate the magnetic data analysis. The oscillations are seen to be in-phase out to the radius at which they become too small to be detected. The likely interpretation is that the plasma displacement at radii outside the resonant q=2 surface is much smaller than at radii inside the surface. This situation commonly occurs for tearing modes on the low field side and the interpretation is supported by a toroidal stability calculation using the FAR code with an approximation to the observed equilibrium. The resulting solution is shown in figure 18 where magnetic surfaces are shown corresponding to $\delta B_\theta/B_\theta = 3\times10^{-3}$ at the plasma surface. It is seen that the m=2, n=1 out-of-phase amplitude is comparatively small in amplitude and radial extent.

Since the electron temperature fluctuations are seen to be associated with the magnetic perturbations it is reasonable to assume that in the deformed state the spatial variation of the electron temperature will indicate the presence of magnetic islands. Thus if the temperature were constant on magnetic surfaces within a magnetic island, the temperature across the island would be flattened, at least in the sense that the temperature of a flux surface on opposite sides of the island would be equal. To investigate this the electron

temperature profiles were obtained at six different times in shot 11051. These times are shown in figure 19 and correspond alternately to times when the X-point (maximum of B_θ) and the O-point (minimum of B_θ) of a magnetic island lies in the line of viewing of the temperature measurement.

The results are shown as consecutive pairs in the lower part of figure 19. In the first two a tendency towards flattening at the O-point is seen and in the third a clear flattening is apparent. The structure is as expected from the radial variation of the amplitude of the temperature oscillations as discussed above. Thus the third flattened case corresponds to the island shape shown in figure 20(a) rather than the more usual form of figure 20(b). The observation of incomplete flattening for the first two profiles may be due to lack of resolution, the radial resolution of the measurement being ~4cm. It will also be partly due to incomplete temperature equalisation in the neighbourhood of the separatrix.

The present results do not show the existence of cool magnetic islands (hollow temperature across the island) suggested in the thermal instability model for disruptions [36], but they do not rule out some contribution from this effect.

iii) Mode locking

We now consider the question of mode-locking. The observation that when a certain amplitude is reached the frequency falls increasingly rapidly to zero might be explained by the model proposed by Nave and Wesson [37]. In this model the magnetic perturbations, $\tilde{B}_r$, penetrate the vacuum vessel and induce surface currents in the vessel

along the direction of the helix. If the current density is j_s there is a force $j_s \times \tilde{B}_r$. The reaction force on the plasma is in the direction to slow the motion of the magnetic island and the timescale is that required to produce the required change in plasma momentum. Comparison with theory [35] indicates that only the toroidal component of the acceleration appears and that the mass involved is intermediate between that of the plasma inside the magnetic island and that of the whole plasma.

Mode-locking occurs at values of $\tilde{B}_\theta$ at the wall of 4-20 gauss and B_r outside the wall of 0.25-1.5 gauss. In a typical case this value corresponds to an m=2 island width $\sim$ 8cm. At the time of the final disruption the radial magnetic field has grown to a value $\tilde{B}_r(n=1)/\ B_\theta(\text{wall}) \approx 0.6\text{-}1.2\times10^{-2}$ and the calculated island width is $\sim$ 25cm.

iv) Minor disruptions

The growth of the magnetic fluctuations following mode-locking leads to a sequence of minor disruptions before the final hard disruption. The magnetic behaviour for shot 11051 was shown in figure 16. We shall now look at the behaviour of the electron temperature during this time. The measurements were made with a 12 channel grating polychromator with the line of sight shown in figure 3.

Figure 21 shows the electron temperature at R = 3.74 and 3.99m. After the time 8.07s the temperature exhibits successive flattenings and comparison with figure 16 shows these flattenings to be correlated with times of growth of $\tilde{B}_r$ (n=1), indicating that they can be

attributed to the growth of m=2, n=1 islands.

Figure 22 presents a more detailed examination of the minor disruption behaviour for shot 11050 (which is similar to shot 11051). It shows the electron temperature at three radii, contours of equal soft X-ray signal plotted against major radius and gives the amplitude of the n=1 component of the locked magnetic field, $\tilde{B}_r$ (n=1). On the graph of the magnetic field amplitude an estimate of the corresponding m=2, n=1 island size is also given.

Three flattenings of the electron temperature profile occur at times indicated by arrows on the $\tilde{B}_r$ trace. The first two flattenings take 3 and 2ms respectively, the third is much faster and has a larger radial extent. These results are consistent with the soft X-ray measurements. The soft X-ray behaviour for the third flattening shows a marked asymmetry and is very similar to the collapse before the final, major disruption. While the first two minor disruptions coincide with an increase in the perturbed magnetic field and therefore the calculated island width, no increase is seen with the third. There are indications that this third flattening is due to an n=2 perturbation.

It seems likely that the minor disruptions are generally explained by a relaxation process [34]. The growth of the m=2 magnetic island results in a fast transport of energy across the plasma radius. The changed conductivity distribution produces a less unstable current gradient around the q=2 surface. This however is temporary and the current profile diffuses back to its unstable form instigating the next minor disruption cycle.

3. Energy Quench

The central event of the disruption sequence is the energy quench, in which most of the plasma energy is rapidly lost. Since, for density limit disruptions, this is usually preceded by what we have called minor disruptions it is natural to refer to the energy quench as a major disruption.

In JET the energy quench proceeds in two stages. The first stage, which is similar to minor disruptions, is observed on the soft X-ray emission. This is shown in figure 23 where the contours of equal signal amplitude are plotted against major radius or height and time. There is a change in the emission which has an m=1, n=1 structure and occurs over about 1ms. However the plasma then settles to an almost symmetric state for a period of about 1ms before the second stage of the energy quench.

Although it might be thought that this first event is an m=1 mhd instability, perhaps related to the sawtooth relaxation, this does not appear to be the case. Figure 24 shows plots of the soft X-ray emission observed across the mid-plane. It is seen that the emission is "eroded" on one side but that initially the other side is unaffected. In an m=1 mhd instability the central part of the emission profile is shifted to one side together with the magnetic axis.

From the ECE temperature measurements it is found that the drop in soft X-ray emission is associated with a fall in temperature and calculations show that the two are consistent. The energy loss during this event can be up to half of the plasma energy.

The second stage of the energy quench is a more rapid event. More than 90% of the remaining electron energy is lost in about 250μs. The precise timescale is unclear because non-thermal emission is usually generated at this time and this complicates the interpretation of the ECE emission. This rapid phase of the disruption is accompanied by a sharp discontinuity in the

amplitude of the n=1 and 2 modes which grow rapidly (∿1ms) to a very much larger amplitude than seen earlier in the disruption sequence.

At this time the soft X-ray emission has a pronounced spike, shown in figure 25. The duration of the spike is typically ∿ 200μs. The increase in X-ray emission occurs across the whole plasma, implying the migration of energetic electrons from the plasma centre to the edge on a very rapid timescale.

Immediately following the energy quench there is a fast decay of the plasma current. It will be shown in the next section that this is consistent with the plasma at that time being cold and impure. It is possible therefore that the soft X-ray spike is caused by the influx of impurity. The duration of the observed spike would then be determined by the cut-off in the detected signal as the plasma temperature fell below the level at which the filter becomes opaque (∿ 500eV). If it is assumed that the soft X-ray emission is due to carbon, a calculation of the rate of carbon influx which would produce the observed signal indicates that the required rate of increase would be such as to double the original level of impurity in 40μs. The carbon impurity level in a normal plasma is typically 2%. The calculated rate of fall of electron temperature resulting from this influx would reduce the electron temperature to 10's of eV in a fraction of a millisecond as is observed.

It seems clear therefore that impurities play a role in the energy quench. In JET the immediate bounding surfaces are carbon and so this is likely to produce the dominant impurity.

4. Current Decay

The physics of fast current decays is complicated by the generation of runaway electrons. However, we shall see that the observed behaviour is consistent with a model in which the high resistance causing the decay

results from a low electron temperature. The impurity radiation at this low temperature gives a power loss of typically $\sim$ 1GW and this is supplied by the rapid ohmic dissipation of the poloidal magnetic field energy of the plasma current.

Figure 26 shows a current trace for a shot in which the plasma current decays from 1.9MA to a plateau at $\sim$ 0.6MA before a rapid final decay. The current during the plateau phase is believed to be carried by runaway electrons. This explains the observed resistance of $\sim 2\mu\Omega$ which is $\sim 10^3$ lower than the ohmic resistance corresponding to the electron temperature at this time. It is also suggested by the observation of hard X-rays during the plateau and by a burst of hard X-rays when the current is finally lost.

It seems likely that the runaway electrons are generated at the time of the temperature collapse. The parameter determining runaway production is ET_e/n [38]. If at the time of the fast temperature collapse we take $E = \eta j$, where j is the pre-existing current density, then $E \propto T_e^{-3/2}$ and the runaway parameter ET_e/n is proportional to $T_e^{-\frac{1}{2}}$. Thus, counter-intuitively the low temperature favours runaway production. Detailed calculations show that the observed current would be generated if the electron temperature falls to a few electron volts.

It is possible to elucidate the plasma behaviour during the current decay by determining the power dissipated and relating this to the power loss. This analysis will be carried out for shot 13339 for which the current trace is shown in figure 27. The initial rapid current decay has $\dot{I} \simeq 200$MA/s. The decay continues down to a runaway current of 0.7MA and this is followed after a brief hesitation by the final decay.

The total power input to the plasma is given by

$$P_i = - \frac{d}{dt} \left(\frac{1}{2} LI^2\right) + \int V B_\theta d\ell. \qquad (3)$$

The first term represents the decay of the magnetic energy and the second gives the inward Poynting flux. More precisely, L is the inductance of this current for the space inside the voltage loops situated around the vacuum vessel, and the integral follows a poloidal path through the voltage loops each measuring a toroidal voltage V, B_θ being the poloidal magnetic field.

Because of the uncertainty in the value of L during this time the power cannot be calculated precisely. However, if the inductance at the onset of the current decay is used, an estimate of the power input can be made.

Using this value, L = 3.4μH, and substituting the measured values into equation (3) gives an initial power P_i = 1.3GW. Before the disruption the power input was 1.4MW. The change in the power input by a factor $\sim 10^3$ shows clearly the change in the plasma properties at the disruption.

In order to calculate the plasma resistance it is necessary to determine how much of the energy input is dissipated. Under normal conditions the resistance could be determined from $P_i = I^2 R_\eta$ but in the fast decay phase a considerable part of the energy input goes to the runaway electrons and the correct equation is then

$$P_i - P_r = (I - I_r)^2 R_\eta \qquad (4)$$

where P_r is the power put into the runaway electrons and I_r is the current which they carry. It is necessary therefore to calculate P_r.

The power input to the runaway particles is

$$P_r = \int j_r V \, dS$$

where j_r is the runaway current density and the integral is over the

poloidal cross-section. The runaway current distribution is not known but is likely to be peaked around the centre of the plasma. The voltage at the centre of the plasma is given by

$$V = - L_\phi \frac{dI}{dt}$$

where L_ϕ is the flux inductance of the plasma current. Thus, an estimate of the power input to the runaway electrons is given by

$$P_r = - L_\phi I_r \frac{dI}{dt} .$$

For a less peaked runaway current the effective value of L_ϕ would be lower leading to a lower P_r. An estimate of the maximum L_ϕ gives 4.4μH and for a runaway current of 0.7MA and a current decay rate of 200MA/s this gives $P_r \approx 0.6$GW. To allow for some radial spread in the runaway current we shall take $P_r = 0.5$GW.

The resistance of the plasma may now be obtained from equation (4) using the values obtained above, that is $P_i = 1.3$GW, $P_r = 0.5$GW, $I = 1.8$MA and $I_r = 0.7$MA, and the result is $R_\eta \approx 660\mu\Omega$. This is to be compared with a pre-disruption plasma resistance of $\sim 0.4\mu\Omega$ and represents an increase by more than a factor 10^3.

Using the value of plasma resistance it is now possible to make an estimate of the plasma temperature, assuming the resistivity to be due to Coulomb collisions. The cross-sectional area, A, of the plasma is $\sim 6m^2$ and its length, ℓ, is ~ 19m. The average resistivity, given by $\eta = AR_\eta/\ell$, is therefore $6\times660\times10^{-6}/19 = 2.1\times10^{-4}\Omega$m. Equating this to the Spitzer resistivity, $\eta = 6.6\times10^{-4} Z_{eff} T_e(eV)^{-3/2}$, gives the electron temperature

$$T_e = 2.1\ Z_{eff}^{2/3}\ (eV).$$

Remembering the temperature dependence of Z_{eff}, the consistent solution of this equation gives a very low temperature, < 10eV, and a small Z_{eff}. The value of Z_{eff} is dependent on the impurity, but at this low temperature is probably around 3. There are of course many uncertainties, including the area of the current channel and the possibility of non-ohmic impedance. However the indication is that the electron temperature is very low.

Direct measurement of the temperature at this time is difficult. The electron cyclotron emission falls to a very low value. This could be due to a cut-off as a result of an increase in electron density to a value $\gtrsim 2\times10^{20}m^{-3}$. Alternatively it indicates a fall in electron temperature to a value less than 30eV.

A possible explanation of these results is that the electron temperature is kept at a low value $\sim$ 10eV by intense impurity radiation. To explore this possibility we shall make an estimate of the impurity level required to radiate the ohmic part of the input power. Since the initial input power is 1.3GW and the estimated power input to runaway electrons is 0.5GW, the ohmic power is approximately 0.8GW.

The coronal radiated power is given by

$$P_R = n\ n_I\ \rho\ V$$

where n and n_I are the electron and impurity densities, $\rho(T_e)$ is the radiation parameter and V is the plasma volume ($\sim$ 110m²). For T_e around 10eV the values of ρ for the possible impurities lie in the range 10^{-32}-$10^{-31}Wm^3$ and, taking the radiated power equal to initial ohmic power, that is 0.8GW, the fractional impurity concentration, $f = n_I/n_H$, is given

approximately by

$$f(1 + f\bar{Z}) = (1\text{-}10)\ \left(\frac{10^{19}}{n_H}\right)^2 \qquad (5)$$

where n_H is the hydrogen density and $\bar{Z}$ is the mean impurity ion charge. The hydrogen density at the time of the energy quench is not known. At the onset of the disruption it was $\sim 1.4 \times 10^{19} m^{-3}$. Substitution of this value into equation (5), with $\bar{Z} = 3$, gives f in the range 30% to 100% indicating that the plasma is very impure and may consist largely of impurities.

It is clear that if the above account of the current decay is correct, a very large power should be recorded by the bolometer. However, the time resolution of the bolometer array is 20ms and the power cannot be resolved on the time of the current decay. It is nevertheless possible to make a comparison of the total energy dissipated with the integrated power measured by the bolometers. Using the integrated forms of equations (3) and (4) the total energy input during the complete current decay is approximately 7.5MJ. Of this approximately 3MJ is given to the runaway electrons. If this runaway energy is transmitted directly to the surrounding surfaces, the energy to be expected in the form of radiation is $\sim$ 4.5MJ.

For shots having the same conditions as the one under consideration, the total energy measured by the bolometer during the disruption current decay shows a variation up to a factor 2, indicating perhaps a lack of toroidal symmetry in the radiation. For the present shot the total radiated energy, assuming toroidal symmetry, is found to be $\sim$ 8MJ. This is almost twice the dissipated power. However, despite the uncertainty it is seen that it is quite likely that the very large dissipated energy is indeed lost in impurity radiation.

For slower current decays a more precise comparison is possible, firstly because the bolometer can resolve the time dependence and secondly because runaway electrons are not significant. The time dependent behaviour for such a case is shown in figure 28. It is seen that in this case the dissipated energy can be accounted for by radiation.

Turning now to the brief current increase which occurs just before the current decay, figure 29 gives a more complete picture of the behaviour for shot 13505. Coincident with the period of increased current is a negative voltage spike which is typically more than a hundred times the positive voltage required to drive the normal current.

The negative voltage spike has usually been attributed to an mhd process in which the current profile undergoes some degree of flattening as a result of current gradient driven tearing modes. To the extent that magnetic energy $\frac{1}{2}LI^2$ is conserved in this process the resulting lower inductance is manifested in a current increase. The positive $\dot{I}$ then produces the negative voltage spike in the voltage loop. In this model the mhd behaviour changes the magnetic topology and this causes the disruptive energy loss. (The process may alternatively be described in terms of an expulsion from the plasma of poloidal flux) [39].

The JET experiments as illustrated by figure 29 raise questions concerning this model because the current increase and negative voltage spike <u>follow</u> the energy loss and would not appear to be part of the process causing the loss. There will be induced voltages as the major radius of the plasma adjusts to the change of β_p. However, although the displacement of the plasma would produce a negative voltage spike on the inner (smaller R) side of the plasma where the poloidal flux is compressed, the corresponding <u>expansion</u> of magnetic flux on the outer (larger R) side of the plasma would produce a positive voltage. It is however usual on JET for a negative

voltage to be measured on all of the voltage loops around the plasma, indicating that the plasma displacement makes only a small contribution to the voltage.

III LOW q DISRUPTIONS

The low q disruptions differ from density limit disruptions mainly in the absence of the extended precursor activity and soft-disruptions. They typically exhibit a fast rise of the n=1 perturbed magnetic field $\sim$ 10-20ms before the energy quench and a mode lock during this time. Figure 30 shows the behaviour of the magnetic perturbations and the H_α signal for a 3.5MA discharge with $q_\psi = 2.0$. Sawteeth are observed until the energy quench.

The energy quench is similar to that of density limit disruptions, almost all of the energy being lost, leaving a low temperature plasma. This leads to the onset of a rapid current decay which can be similar, but generally slower, than that of a density limit disruption. However, for low-q disruptions where the density is lower and radiation does not play a significant role in producing the disruption, a different type of current quench is often observed. In these cases a recovery from the temperature collapse occurs during the current decay. Such a case is shown in figure 31. It is seen that the temperature rises to 2/3 of its original value and rate of current decay falls accordingly. The discharge is finally brought to an abrupt end by a second disruption. The rate of current decay during the reheat period is consistent with the measured temperature for $Z_{eff} \sim 7$. This is consistent with a plasma strongly contaminated with carbon (the material of the limiter and inside wall) or oxygen. If the same amount of impurity is assumed at the time of the initial rapid current decay (decay time 80ms at 11.6s) the calculated mean electron temperature is $\sim$ 10eV with $Z_{eff} \sim 3$. This is again consistent with the observed electron cyclotron emission.

IV CURRENT RISE DISRUPTIONS

The variety of mhd activity during the current rise has been classified in terms of q_a - q_o space [40] or the empirical ℓ_i - q diagram [35] shown in figure 6 which is similar to the diagram computed in ref.[41]. The JET results are summarised below.

In the region $q_a > q_o$ or $\ell_i < 0.5$, where double tearing modes could be important, the mhd activity shows broad peaks in time but no clear correlation with q. The magnetic equilibrium analysis shows that abrupt redistribution of the plasma current can occur on timescales shorter than expected from thermal transport and cause the current profile to become more peaked.

In the region $1 < q_a/q_o < 2$, or just below the jagged lower boundary of figure 6, where surface kink modes are expected to occur, the mhd activity is sharply correlated with q_a and has mode numbers n=1, m=q. Even though the amplitude of $\dot{B}_\theta$ is often large, such activity disappears as q_a drops below the rational value and does not disturb the gross parameters of the discharge provided $\tilde{B}_\theta$ is not too large.

For more peaked current profiles, a stable region is normally encountered. For yet more peaked profiles sawteeth appear and, finally, in the vicinity of the upper boundary of figure 6 density limit disruptions occur.

If the instability amplitude reaches $\tilde{B}_\theta$ = 4-20G, its toroidal rotation velocity is reduced and the mode becomes almost stationary - the so called quasi-stationary mode or QSM [35]. This mode sometimes grows explosively and produces a prompt disruption. Alternatively it can die away or recommence rotating. The mode can also persist for many seconds even if changes in ℓ_i or q bring the discharge into the normally stable region. If the current ramp is continued with such a QSM present the plasma will suffer

a major disruption at a lower integer value of q_a, often at $q_a = 3$. If the current ramp is decreased the QSM will sometimes continue to grow and a major disruption occurs near the upper boundary of figure 6. This disruption has the usual n=1, m=2 or 3 precursor but no radiative collapse. In this way the QSM provides the link between the rotating mhd activity characteristic of the current rise and the major disruption. In order to avoid the disruptions associated with the current rise it is sufficient to avoid or suppress the QSM. This is done by steering the discharge through the ℓ_i-q diagram by careful control of current ramp rate, minor radius, elongation and density so as to enter the stable region in figure 6. This is particularly important in order to obtain discharges below $q_a = 3$.

Figures 32-35 show data from a JET shot selected to illustrate some of the features summarised above. It should be noted that the details vary considerably for different pulses depending on the trajectory through the ℓ_i-q plane. Figure 32 shows this particular discharge spends the first second or so in the region of the ℓ_i-q plane where either double tearing modes or surface kinks might be important. Note the jumps in ℓ_i at near integer values of q, which are well correlated in time with the mhd peaks shown in figure 33. The electron temperature data included in this figure shows relaxations on timescales <1ms at a minor radius of about 0.4m but no change near the axis.

During this time several such relaxations occur but the current profile calculated from magnetic equilibrium analysis remains distinctly hollow with steep edge gradients as shown in figure 34. The mhd fluctuations are predominantly n=1 with strong n=2 and 3 components, but given the nature of the current profile these could be either surface or internal modes. At 0.9s a QSM appears and there is a further jump in ℓ_i and, as expected from flux conservation, a temporary hesitation in the current rise. The QSM grows in amplitude with occasional abrupt changes in amplitude and phase

with associated rapid drops in the electron temperature at half radius. At 1.37s the electron temperature drops in <1ms both near the axis and at half radius and the current profile shown in figure 34 makes an abrupt transition from hollow to peaked. The q profile shown in figure 35 changes from having minima in the outer regions of the plasma to having a minimum near the axis. This transition takes the discharge into the normally stable region of the ℓ_i-q diagram as seen in figure 32, but the QSM still grows. At 2s into the discharge there is a minor disruption accompanied by a positive current spike and a flattening of the current profile. The rotating mhd which follows this minor disruption decays away but the QSM persists for a further 2s eventually leading to a major disruption.

V SUMMARY OF EVENTS

In order to bring together the various events which have been described, we give three tables. In the first two the time sequence of events for density limit and low-q disruptions are presented diagramatically. In the third the time of occurrence and time duration of the events in a density limit disruption are given together with possible explanations of each event.

DENSITY LIMIT DISRUPTION SEQUENCE

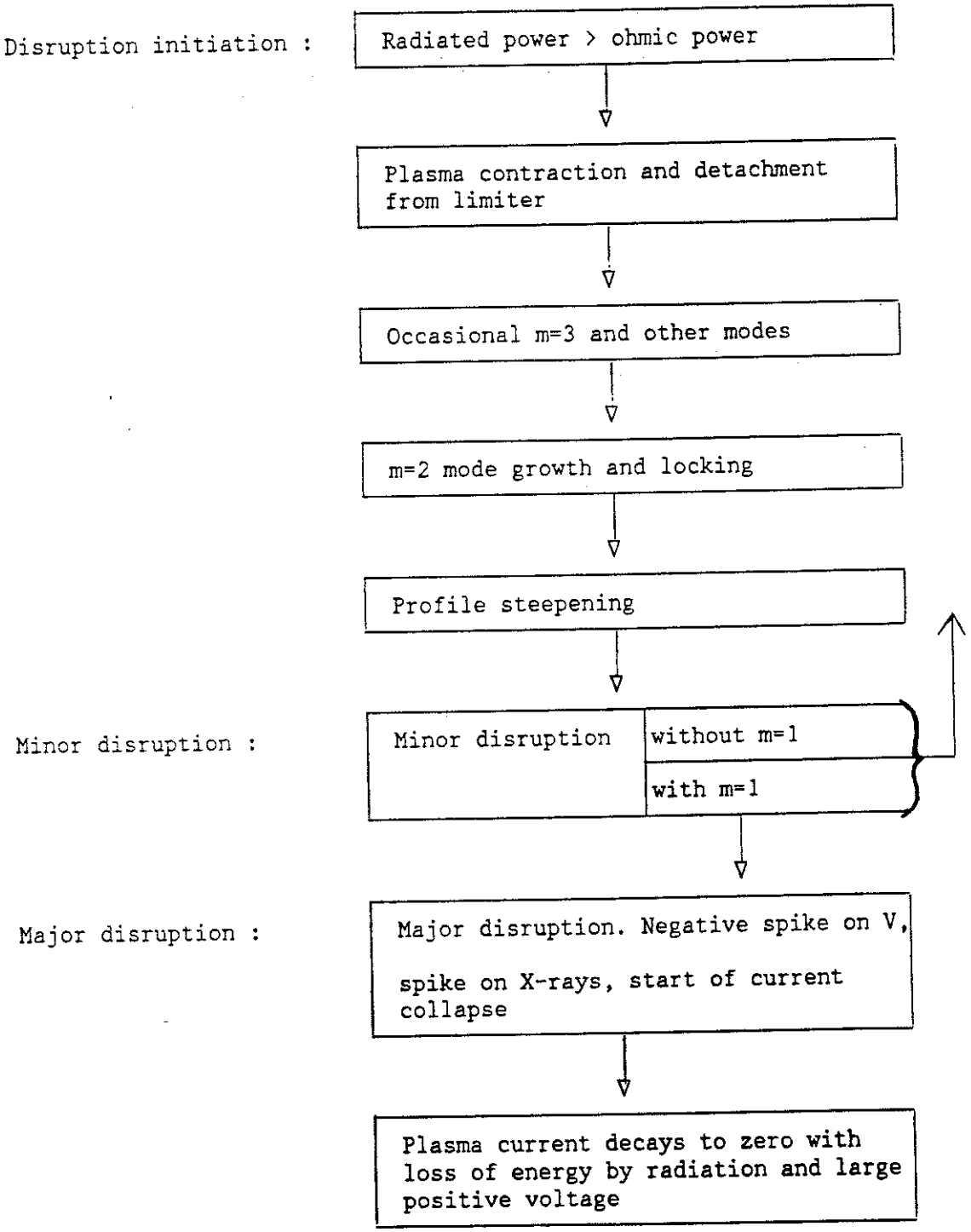

LOW-q DISRUPTION SEQUENCE

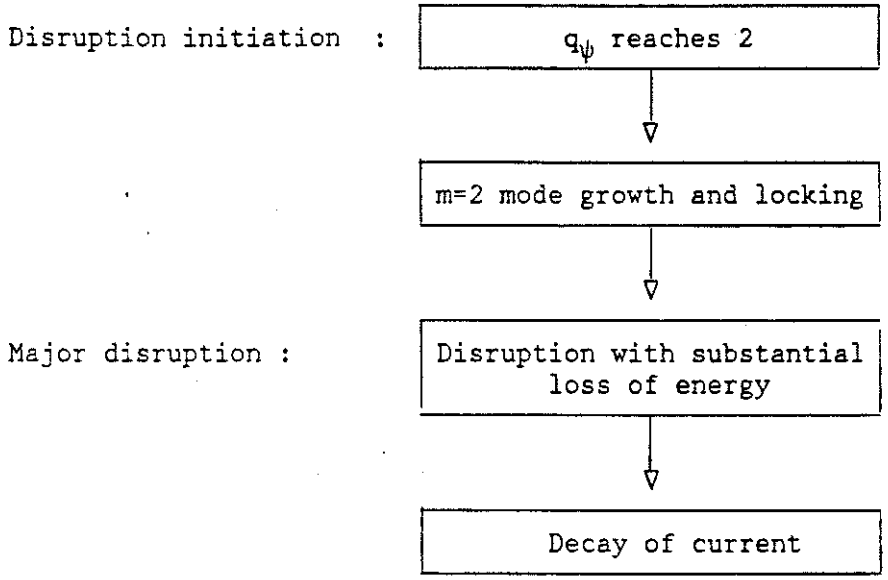

TYPICAL TIMESCALES DURING DENSITY LIMIT DISRUPTIONS

	Time of onset before major disruption (ms)	Timescale (ms)	Possible explanations
Contraction of profile	1,000	500	Radiation cooling of outer plasma
Growth of m=2	200	10	Current profile unstable to tearing modes
Locking of m=2	200		Electromagnetic coupling to vacuum vessel
Soft disruption	various	2	Island growth leading to changed magnetic field topology which is relaxed by the instability
m=1 erosion	2	0.5	Partial disruption with large m=1 island already present
Rapid energy loss	$\sim$ 0.2	0.2	i) Rapid transport due to changed magnetic field structure ii) Influx of impurities
Current decay	0	20	Impure, low temperature plasma
Growth of runaways	- 15	10	High loop voltage

VI DISCUSSION

For the JET tokamak, like all other tokamaks, disruptions place limitations on the operating space. The density is limited because at high densities the increased impurity radiation causes a contraction of the plasma leading first to an mhd unstable configuration and then to an energy loss leaving an irretrievably impure and cold plasma. The q-value is limited at low-q by a rather precise $q_\psi = 2$ boundary but generally little difficulty is experienced in reaching this value. The corresponding cylindrical q value is typically ~ 1.5. Disruptions can also be caused by too rapid a current rise at the beginning of the pulse.

The low-q disruptions have none of the extended precursor and soft-disruption behaviour of density limit disruptions. There is a sudden growth of mhd instability leading to a fast energy quench and current decay similar to those of a density limit disruption. The rather precise limit of $q_\psi = 2$ calls for an explanation since non-linear mhd theory predicts strong instability over a range of q_ψ around $q_\psi = 2$. It might be that the observation is explained by the conjecture of Bondeson [42] that in JET a loss of the stabilising effect of the vacuum vessel occurs as the $q_\psi=2$ surface passes out of the plasma.

The disruptions which are associated with the current rise phase can have a very distinctive character arising from the mhd associated with flat or even hollow current profiles. The final disruptions in these cases is often associated with a peaked current profile but this is not caused by a radiative collapse.

The density limit disruptions bear out the suggestions of Gibson [10], and Rebut and Green [25]. Gibson conjectured that 100% radiated power would be the critical point for a disruption and Rebut and Green described how a radiating layer would form at the plasma surface. The observed contraction which results from this is similar to that described by Ashby and Hughes

[30] except that the radiation occurs at a temperature which is an order of magnitude higher than that predicted for coronal radiation.

The contraction of the plasma temperature takes place on an energy confinement timescale as predicted and leads to growing mhd instability, principally m=2, and to repeated minor disruptions. The magnetic measurements indicate magnetic islands which are sufficiently large to cause the energy loss associated with these minor disruptions and the electron temperature measurements show the expected radial flattening of the temperature profile.

Initially the mhd perturbations appear as oscillations because the mode travels around the torus. At a critical amplitude the oscillations cease but the mode amplitude continues to grow. This process is called mode locking and appears to be consistent with the model of Nave and Wesson in which the moving magnetic perturbations induce currents, and hence a force, in the vacuum vessel [37]. The opposing force in the plasma then brings the magnetic islands to rest.

The final phase, or major disruption, is less well understood. After several minor disruptions during a period of typically 1s, there is a sudden loss of plasma energy from the central region, the affected region having an m=1, n=1 structure. This event, which typically lasts $\sim$ 1 ms, is followed first by a period of quiescence and then by a very rapid loss of almost all of the remaining plasma energy. During this very rapid phase lasting typically 200μs there is a rapid increase in the soft X-ray signal and this is found to be consistent with a rapidly increasing impurity level.

The negative voltage spike which is frequently reported as an event associated with the disruption instability is also seen on JET. However in JET it <u>follows</u> the energy quench and would not therefore seem to be a part of the instability giving rise to this loss.

Further information on the energy quench phase is deduced from the subsequent current decay. The current decay starts shortly after the energy quench. From the very onset the current decay is consistent with a plasma with an electron temperature the order of 10eV cooled by impurity radiation. It seems possible therefore that impurities play an important role in the energy quench process.

Acknowledgements

The authors would like to thank Drs. R. Bickerton, W. Engelhardt and P. Stott for helpful suggestions and useful discussions.

References

[1] Kadomtsev, B.B., Plasma Physics and Contr. Fusion 26 (1987) 217.

[2] Sauthoff, N.R., von Goeler, S., Stodiek, W., Nuclear Fusion 18 (1978) 1445.

[3] Articles in "Current Disruption in Toroidal Devices". Eds. Lackner, K. and Zehrfeld, H.P. Max-Planck-Institut für Plasmaphysik, Garching. Report IPP III/51 (1979).

[4] McGuire, K.M. and Robinson, D.C., Phys. Rev. Lett. 44 (1980) 1666.

[5] TFR Group, Nuclear Fusion 25 (1985) 919.

[6] Tsuji, S, Nagayama, Y., Miyamoto, K., Kawahata, K., Noda, N. and Tanahashi, S., Nuclear Fusion 25 (1985) 305.

[7] Roberts, D.E., de Villiers, J.A.M., Fletcher, J.D., O'Mahony, J.R. and Joel, A., Nuclear Fusion 26 (1986) 785.

[8] Axon, K.B., Baxter, G.A., Burt, J., Clark, W.H.M., McCracken, G.M., Fielding, S.J., Gill, R.D., Goodall, D.H.J., Hobby, M., Hugill, J., Paul, J.W.M., Powell, B.A., Prentice, R., Reid, G.W., Stott, P.E., Summers, D.D.R. and Wootton, A.J. Plasma Physics and Controlled Nuclear Fusion Research, 1978 (Innsbruck) Vol.1, 51 (IAEA, Vienna).

[9] Niedermeyer, H., et al., Controlled Fusion and Plasma Physics, 1983 (Aachen) Vol.1, 43 (EPS); Max-Planck-Institute für Plasmaphysik, Garching. Report IPP III/90 (1983).

[10] Gibson, A., Nuclear Fusion 16 (1976) 546.

[11] Waddell, B.V., Carreras, B., Hicks, H.R., Holmes, J.A. and Lee, D.K., Phys. Rev. Lett. 41 (1978) 1386.

[12] Sykes, A. and Wesson, J.A., Phys. Rev. Lett. 44 (1980) 1215.

[13] Thomas, P.R. et al., Plasma Physics and Controlled Nuclear Fusion Research, 1984 (London) Vol.1, 353 (IAEA, Vienna).

[14] Wesson, J., Gowers, C., Han, W., Mast, F., Nave, M.F.F., Turner, M. and Watkins, M., Controlled Fusion and Plasma Physics, 1985 (Budapest) Eds. Pocs, L. and Montvai, A., Vol.1, 147 (EPS).

[15] Schüller, F.C., Alladio, F., Campbell, D., Crisanti, F., de Kock, L., Krause, H., Lomas, P., Malacarne, M., Mast, F.K., Nave, M.F.F., Niestadt, R., Noll, P., Piekaar, H.W., Thomas, P.R., Thompson, J., Tonneti, G., Tubbing, B. and Wesson, J., Controlled Fusion and Plasma Physics, 1985 (Budapest) Eds. Pocs, L. and Montvai, A., Vol.1, 151 (EPS).

[16] Campbell, D.J., Christiansen, J.P., Lazzaro, E., Morris, A.W., Nave, M.F.F., Schüller, F.C. and Thomas, P.R., Controlled Fusion and Plasma Heating, 1986 (Schliersee) Eds. Brifford, G. and Kaufmann, M., Vol.1, 268 (EPS).

[17] Campbell, D.J. et al., Plasma Physics and Controlled Nuclear Fusion Research, 1986 (Kyoto) Vol.1, 433.

[18] Bartlett, D.V., Campbell, D.J., Costley, A.E., Kissel, S.E., Nowak, S., Brusati, M. and Lazzaro, E., Controlled Fusion and Plasma Physics, 1987 (Madrid) Eds. Engelmann, F. and Alvarez-Rivas, J.L., Vol.III, 1252 (EPS).

[19] Ward, D.J., Gill, R.D., Morgan, P.D. and Wesson, J.A., Controlled Fusion and Plasma Heating, 1988 (Dubrovnik) to be published.

[20] Mast, K.F. and Krause, H., Rev. Sci. Instrum. 56 (1985) 969.
[21] Snipes, J.A., Campbell, D.J., Haynes, P.S., Hender, T.C., Hugon, M., Lopes Cardozo, N. and Schüller, F.C., Controlled Fusion and Plasma Physics, 1987 (Madrid) Eds. Engelmann, F. and Alvarez-Rivas, J.L., Vol.I, 69 (EPS).
[22] Tubbing, B.J.D., Barbian, E., Campbell, D.J., Hugenholtz, C.A.J., Niestadt, R.M., Oyevaar, Th. and Piekaar, H.W., Controlled Fusion and Plasma Physics, 1985 (Budapest) Eds. Pocs, L. and Montvai, A., Vol.I, 215 (EPS).
[23] Salmon, N.A., Bartlett, D.V., Costley, A.E. and Hugon, M., Controlled Fusion and Plasma Physics, 1987 (Madrid) Eds. Engelmann, F. and Alvarez-Rivas, J.L., Vol.III, 1248 (EPS).
[24] Edwards, A.W., Gill, R.D., Oord, E., Tsuji, S., Fahrbach, H-U., Granetz, R.S., Schramm, G., Weller, A. and Zasche, D., Rev. Sci. Instrum. 57 (1986) 2142.
[25] Rebut, P.H. and Green, B.J., Plasma Physics and Controlled Nuclear Fusion Research, 1976 (Berchtesgaden) Vol.2, 3 (IAEA, Vienna).
[26] Gibson, A. and Watkins, M.L., Eighth European Conference on Controlled Fusion and Plasma Physics, Vol.1, 31 (contributed papers) Prague (1977).
[27] Watkins, M.L., Physics Reports 37 (1978) 111.
[28] Igitkhanov, Yu.L., Kukushhin, A.S. and Stakhanov, I.P., Nuclear Fusion 18 (1978) 415.
[29] Ohyabu, N., Nuclear Fusion 19 (1979) 1491.
[30] Ashby, D.E.T.F. and Hughes, M.H., Nuclear Fusion 21 (1981) 911.
[31] Murakami, M., Callen, J.D. and Berry, L.A., Nuclear Fusion 16 (1976) 347.
[32] Lipshultz, B. La Bombard, B., Marmar, E.S., Pickrell, M.M., Terry, J.L., Watterson, R., Wolfe, S.M., Nuclear Fusion 24 (1984) 977.
[33] Ashby, D.E.T.F. and Hughes, M.H., UKAEA, Culham Lab. Report CLM-R228 (1982).
[34] Turner, M.F. and Wesson, J.A., Nuclear Fusion 22 (1982) 1069.
[35] Snipes, J.A., Campbell, D.J., Haynes, P.S., Hender, T.C., Hugon, M., Lomas, P.J., Lopes Cardozo, N., Nave, M.F.F., Schüller, F.C., JET Report P(88)01 and to be published in Nuclear Fusion.
[36] Rebut, P.H. and Hugon, M., Plasma Physics and Controlled Nuclear Fusion Research, 1984 (London) Vol.2, 197 (IAEA, Vienna).
[37] Nave, M.F.F. and Wesson, J.A., Controlled Fusion and Plasma Physics, 1987 (Madrid) Eds. Engelmann, F. and Alvarez-Rivas, J.L., Vol.III, 1103 (EPS).
[38] Dreicer, H., Phys. Rev. 117 (1960) 329.
[39] Kadomtsev, B.B., Plasma Physics and Controlled Nuclear Fusion Research, 1976 (Berchtesgaden) Vol.1, 555 (IAEA, Vienna).
[40] Campbell, D.J., Christiansen, J.P., Cordey, J.G., Lazzaro, E., Nave, M.F.F., Schüller, F.C. and Thomas, P.R., JET-P(86)46 and to be published in Nuclear Fusion.
[41] Cheng, C.Z., Furth, H.P. and Boozer, A.H., Princeton Report PPPL-2372 (1980).
[42] Bondeson, A., Proc. of Workshop on Theory of Fusion Plasmas, 1987 (Varenna) 303; also Persson, M. and Bondeson, A., ibid 325.

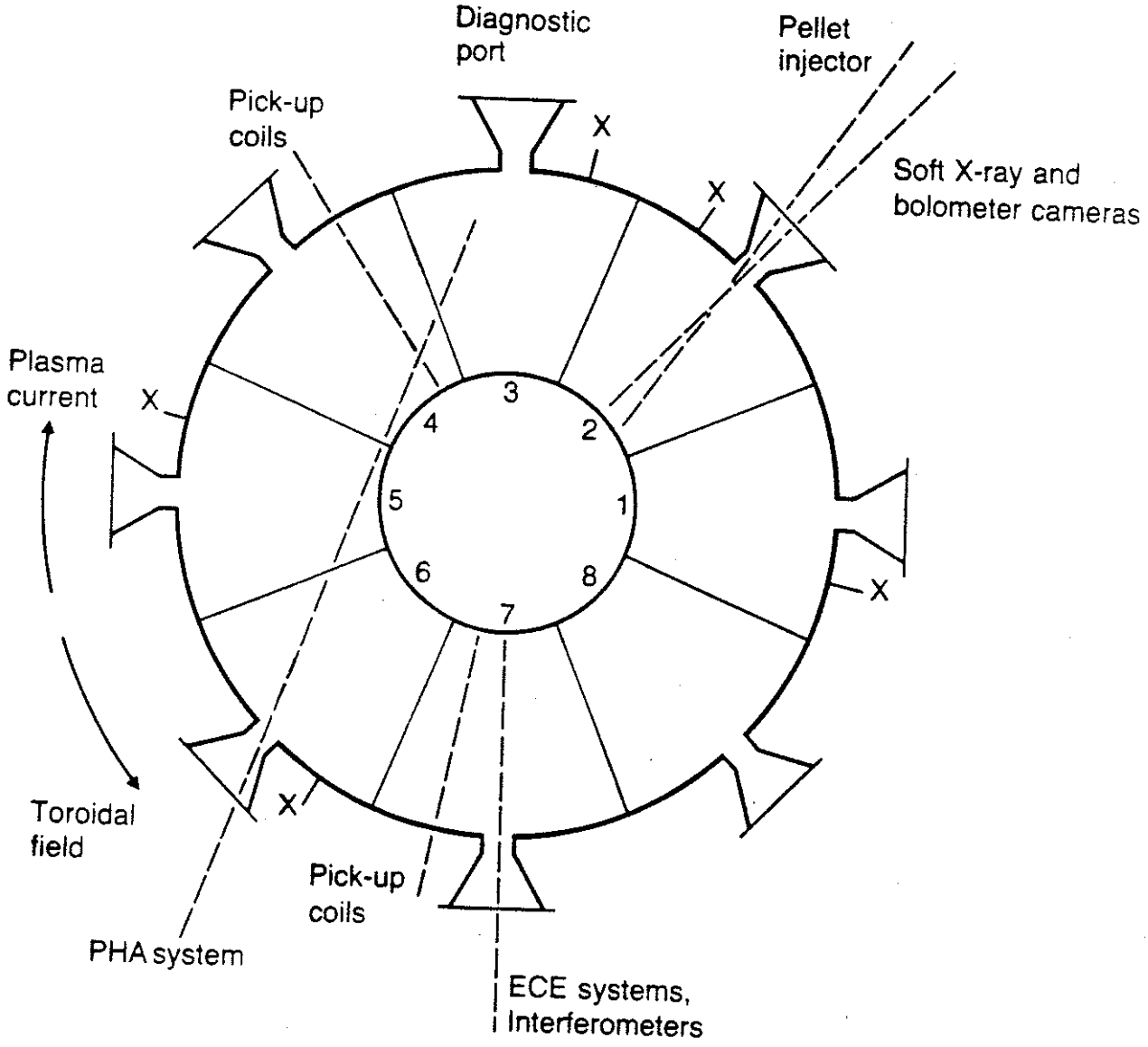

Figure 1 Locations of diagnostics in JET

G88.3/12

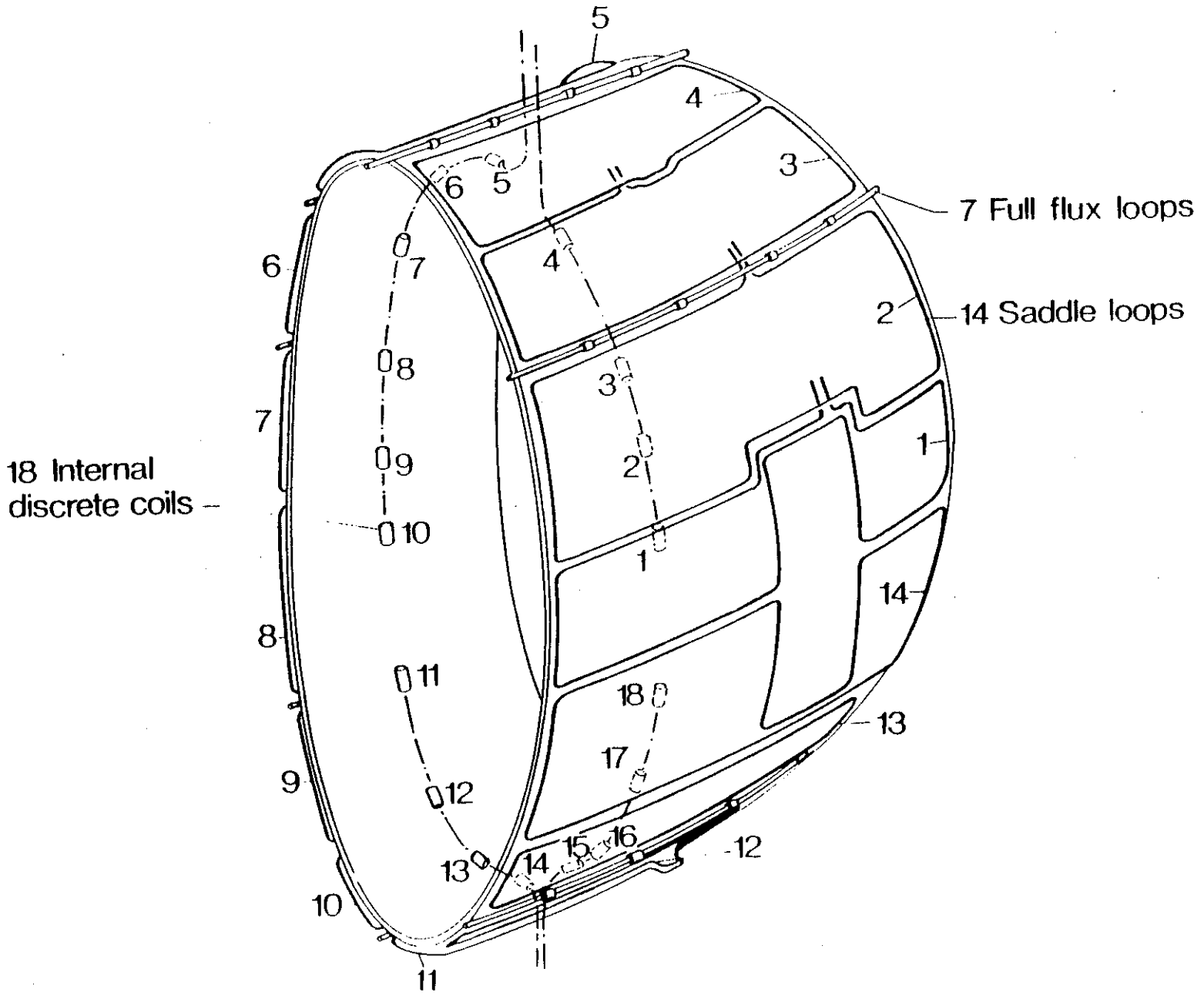

Figure 2 Magnetic diagnostics in a single octant

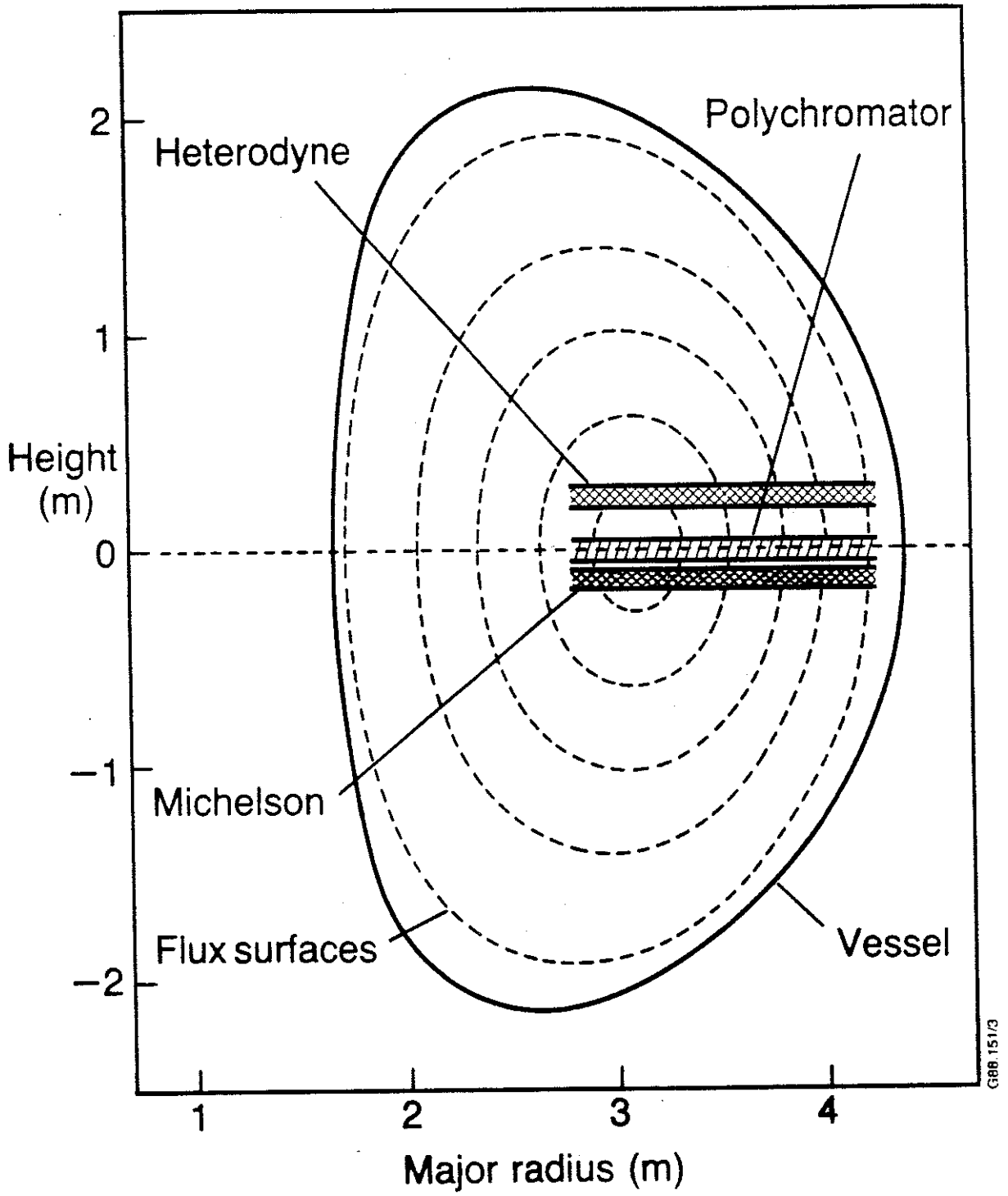

Figure 3 Section of JET showing the viewing zones of the ECE diagnostics. Typical magnetic flux surfaces are also shown

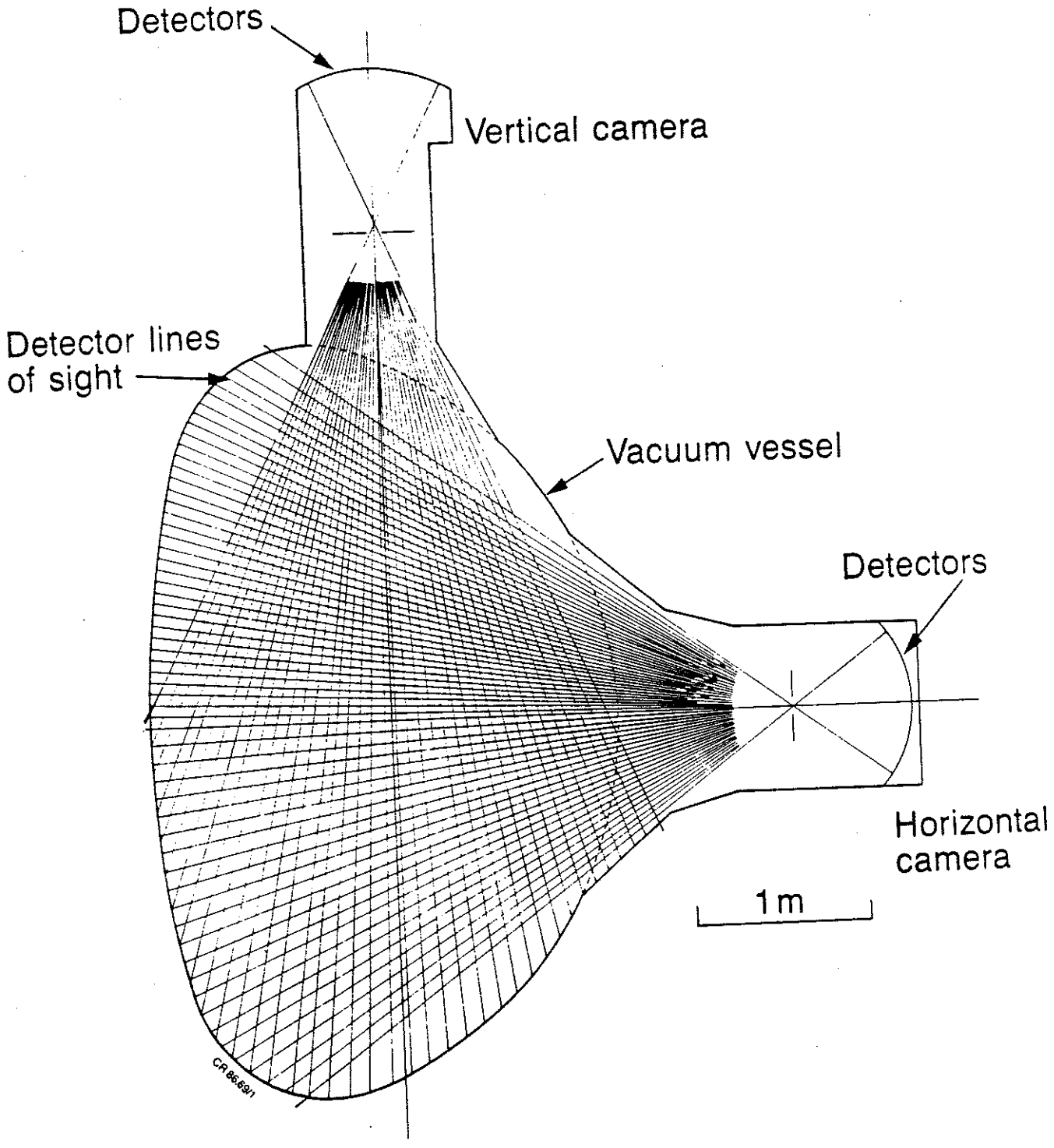

Figure 4 Lines of sight of the vertical and horizontal soft X-ray cameras

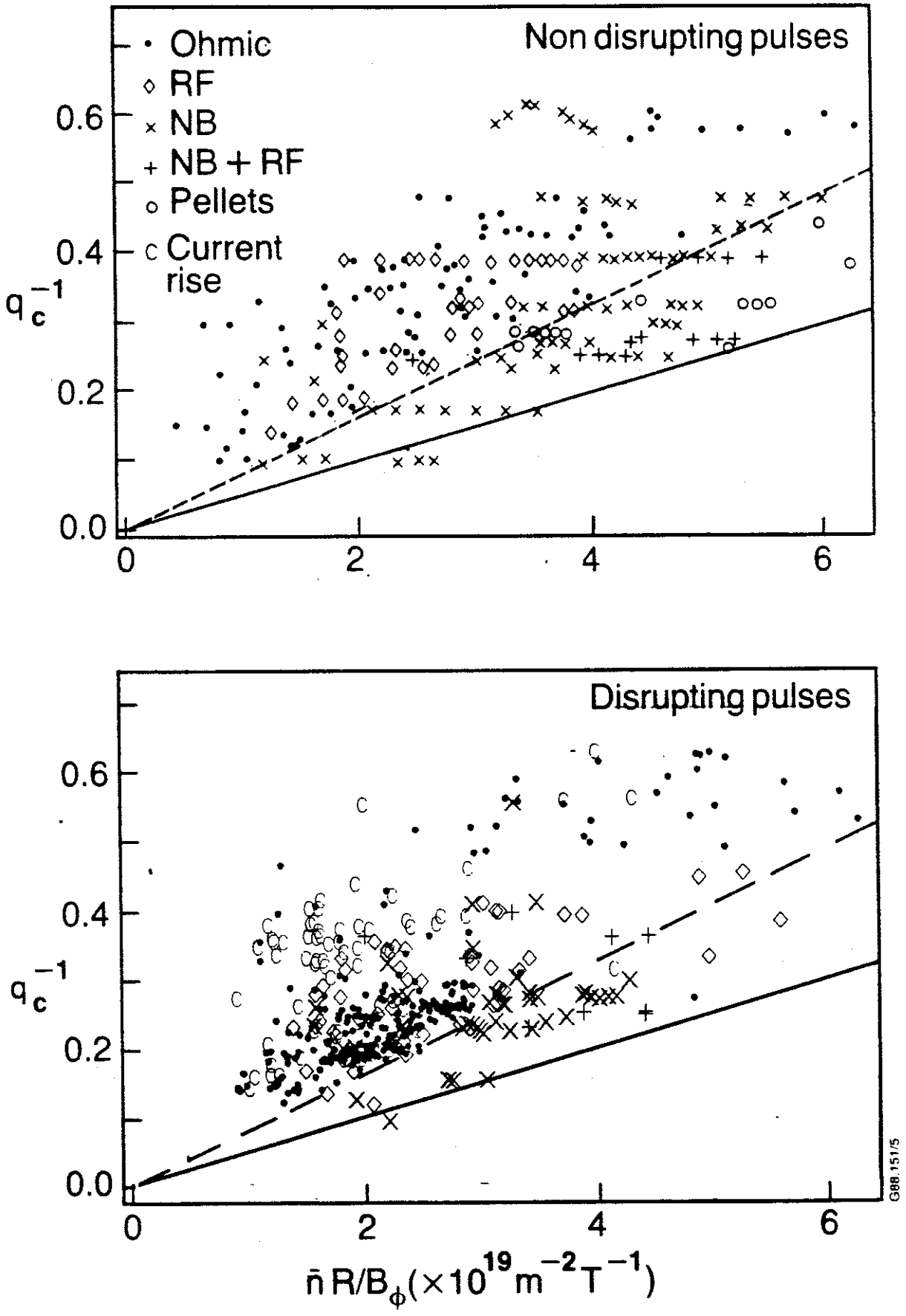

Figure 5 Hugill diagrams showing discharges which (a) did not disrupt, (b) did disrupt. The full line indicates the boundary of operation and the dashed line the boundary for ohmic discharges

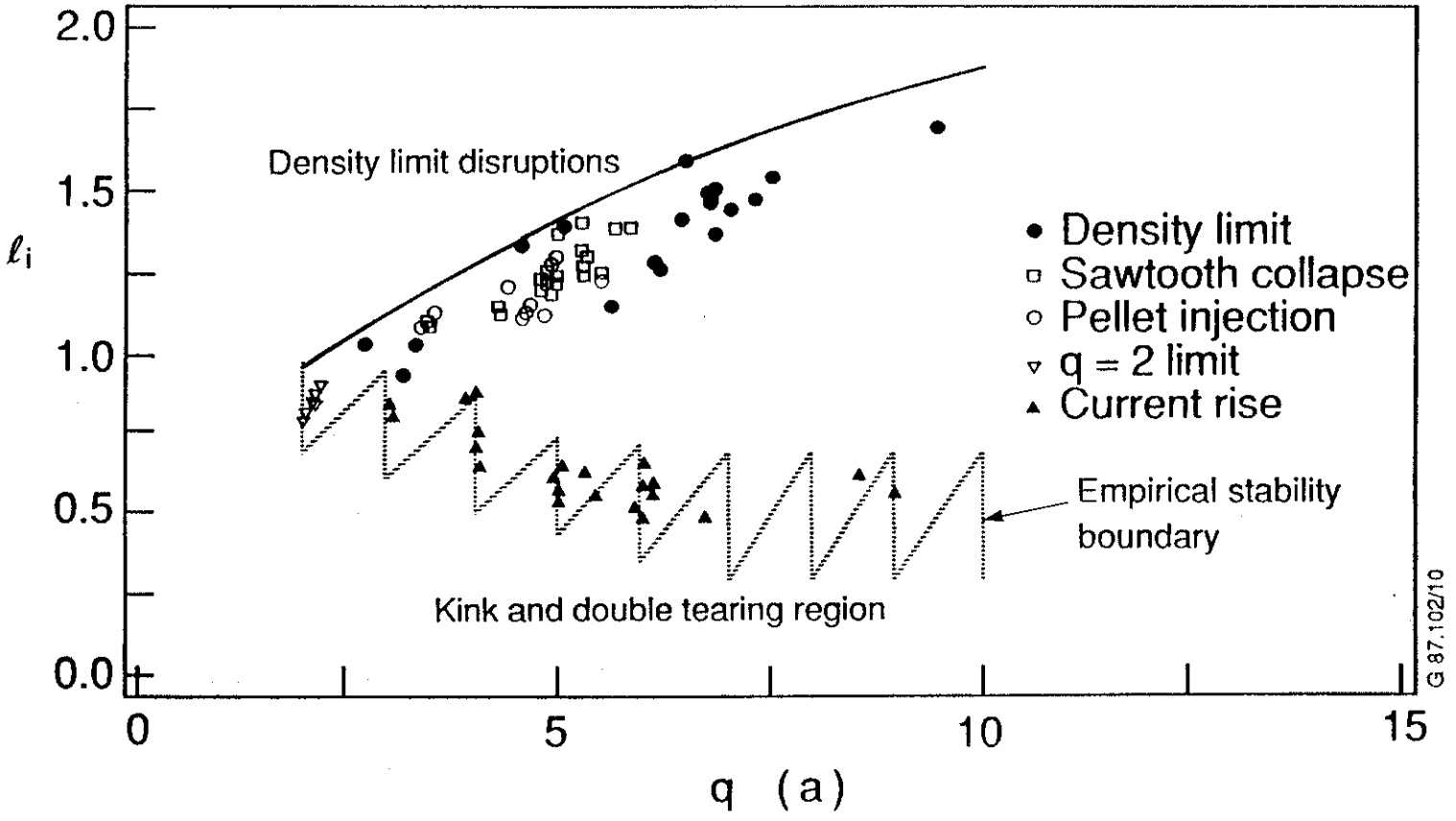

Figure 6 The empirical stability diagram for JET showing the ℓ_i-q plane. The lower boundary (dotted) indicates the stability boundary for rotating mhd during the current rise. The upper boundary (solid) indicates the region where major disruptions occur. The symbols indicate the onset of quasi-stationary modes in various situations

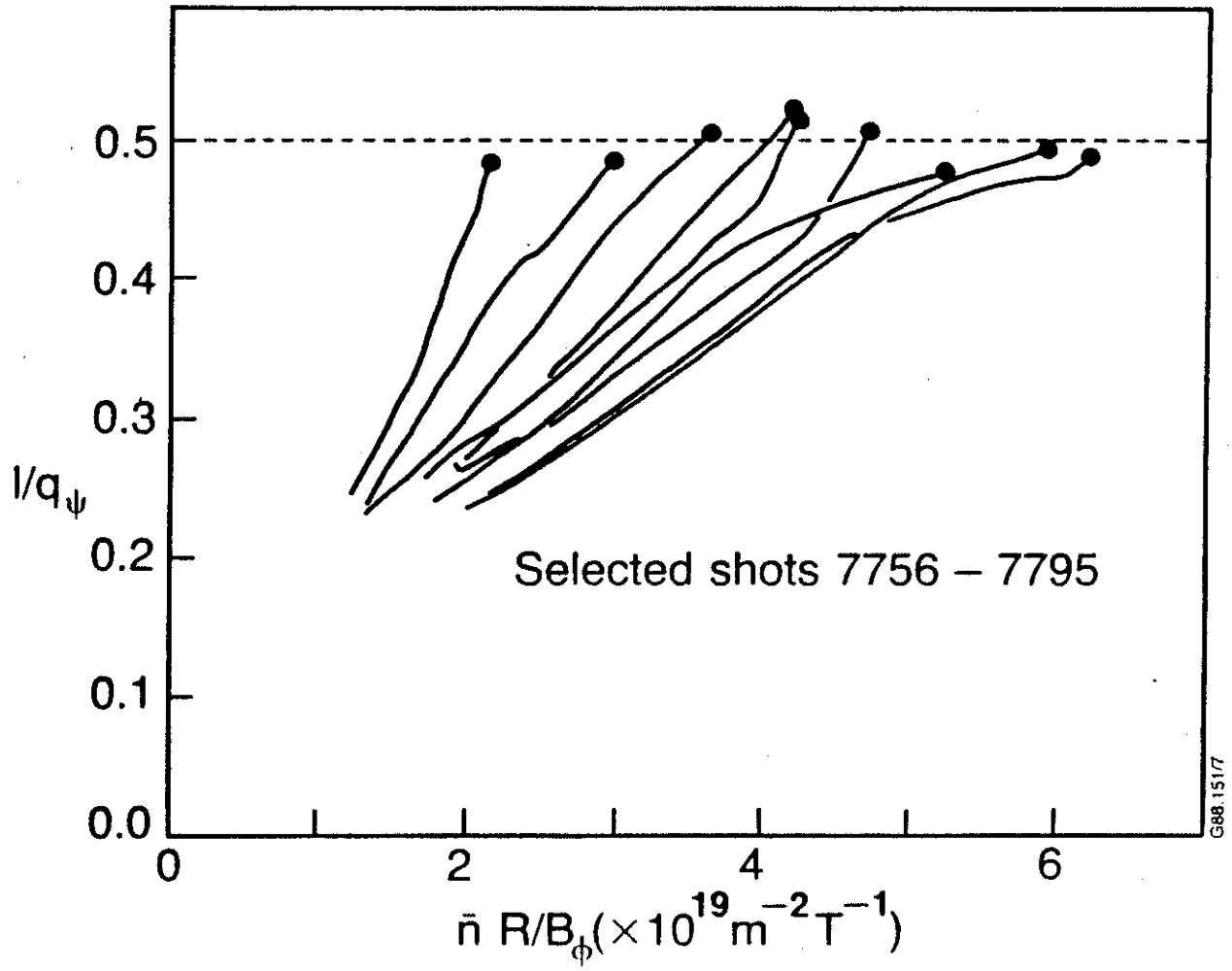

Figure 7 Hugill plot trajectories of discharges which disrupt at low q_ψ

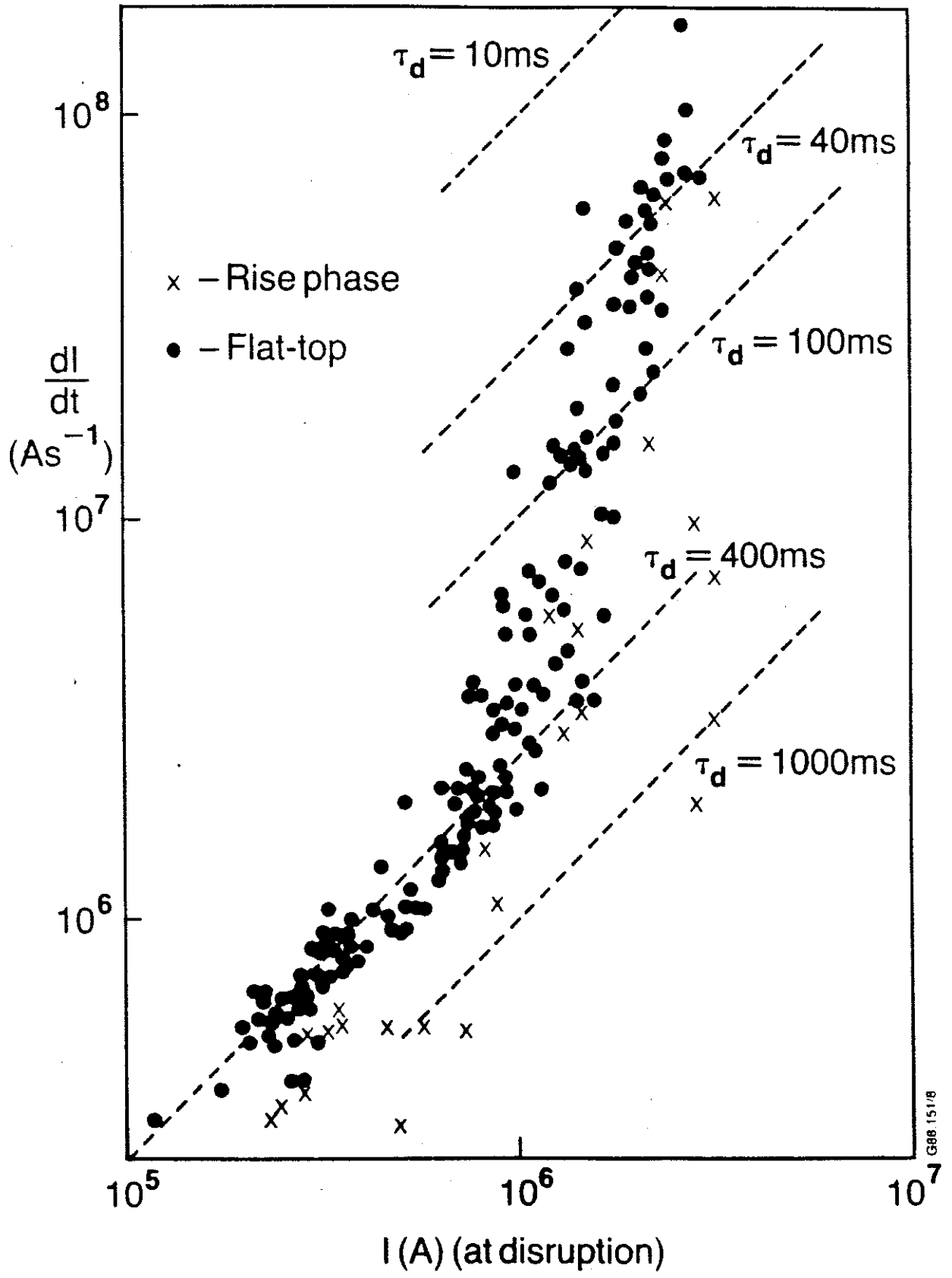

Figure 8 Variation of current decay rate with plasma current

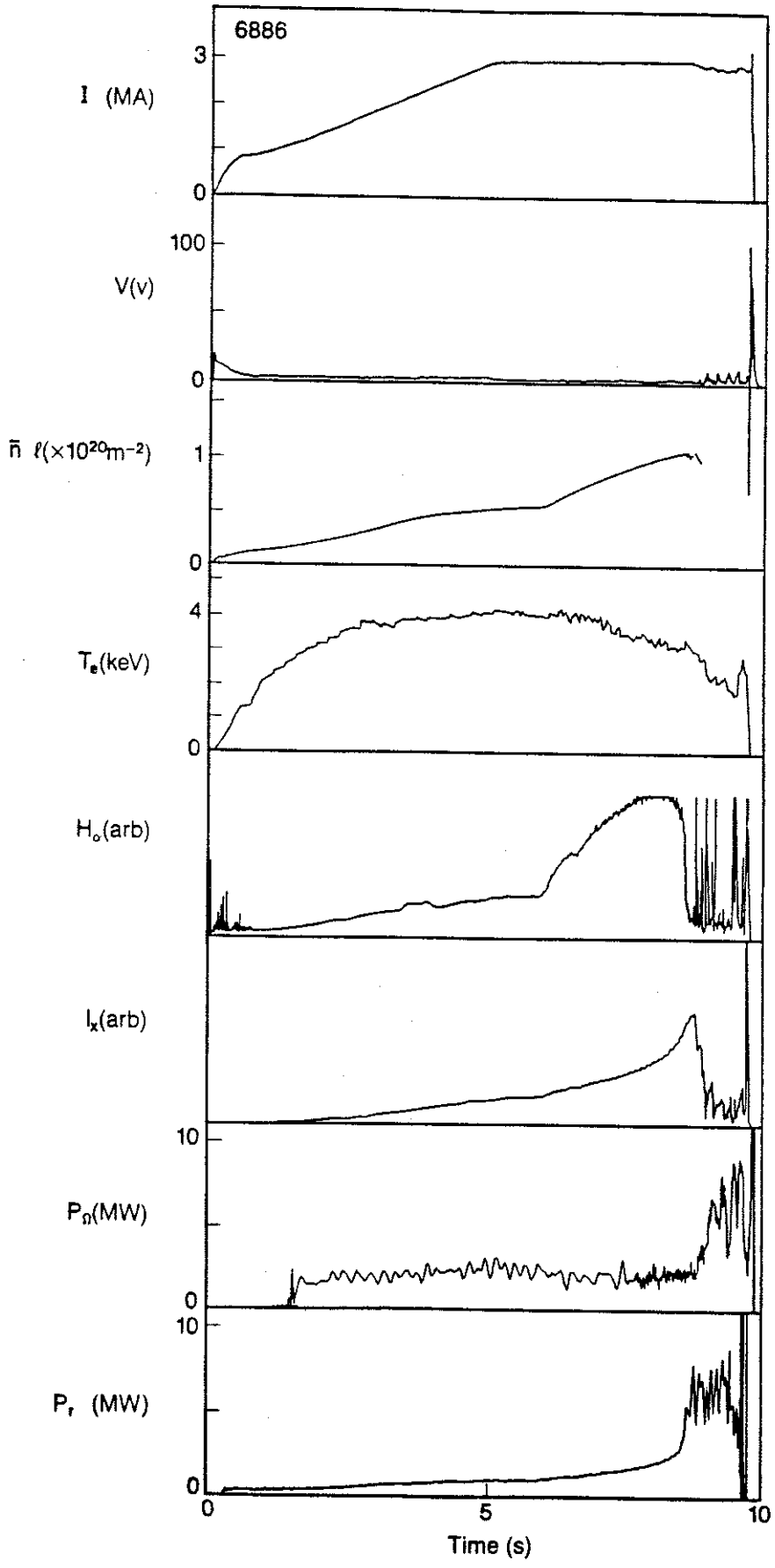

Figure 9 Overview plot of a density limit disruption at t=9.7s. The signals shown are the plasma current, loop volts, line integrated density, T_e, Hα intensity, X-ray intensity (I_x), ohmic power and radiated power

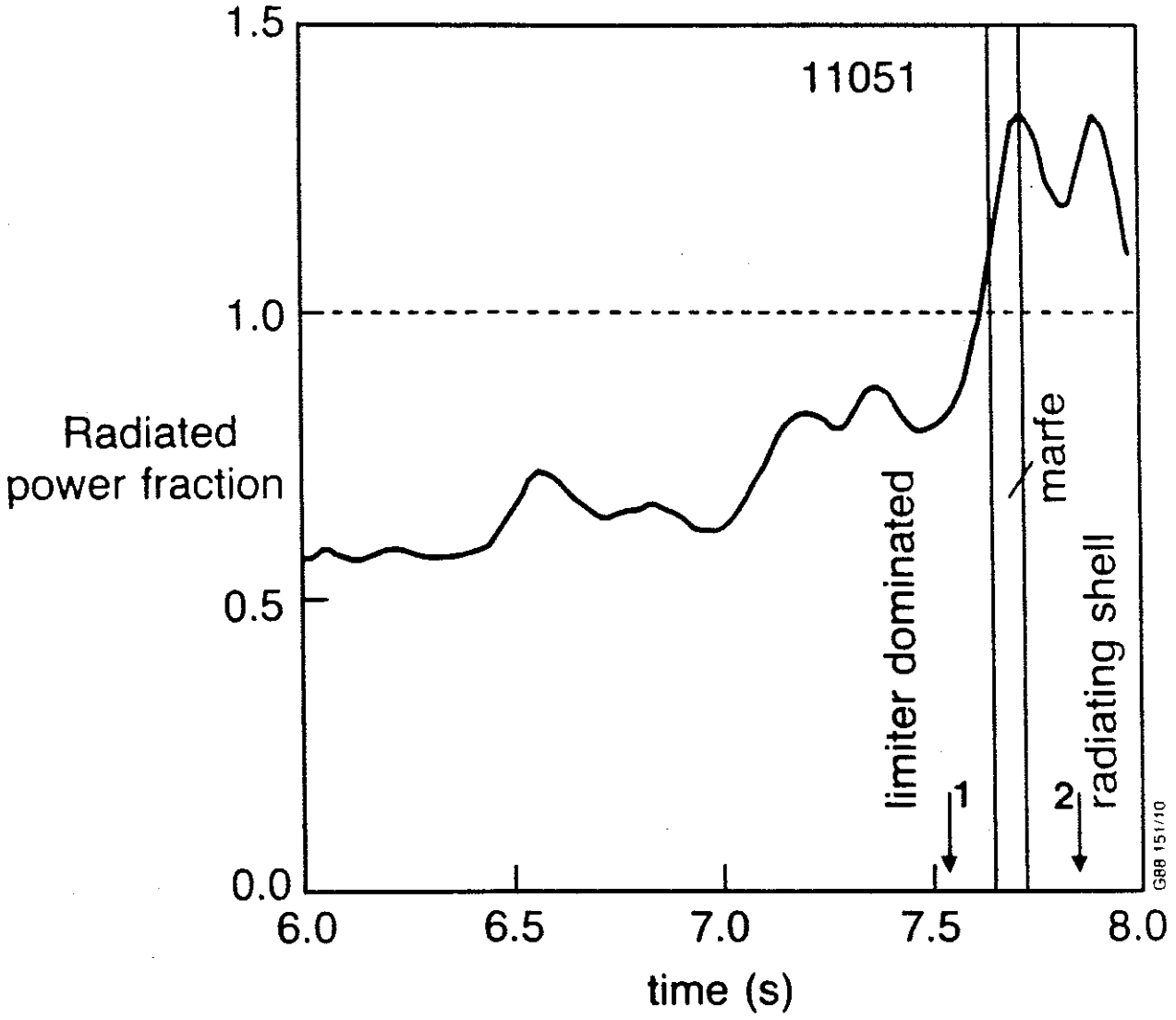

Figure 10 Time dependence of total radiated power fraction

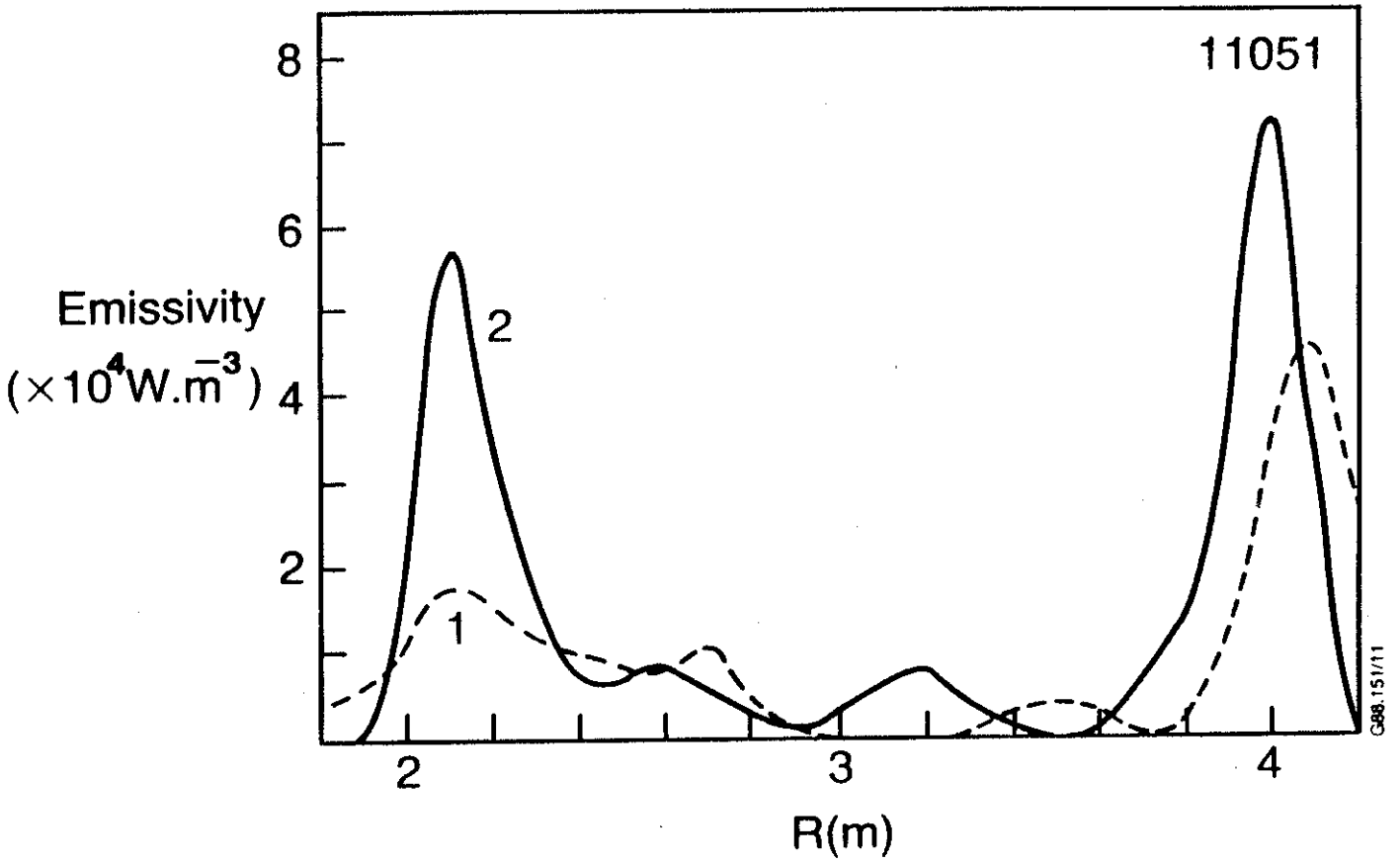

Figure 11 Radiated power radial profiles before (1) and after (2) the radiated power fraction reaches 1

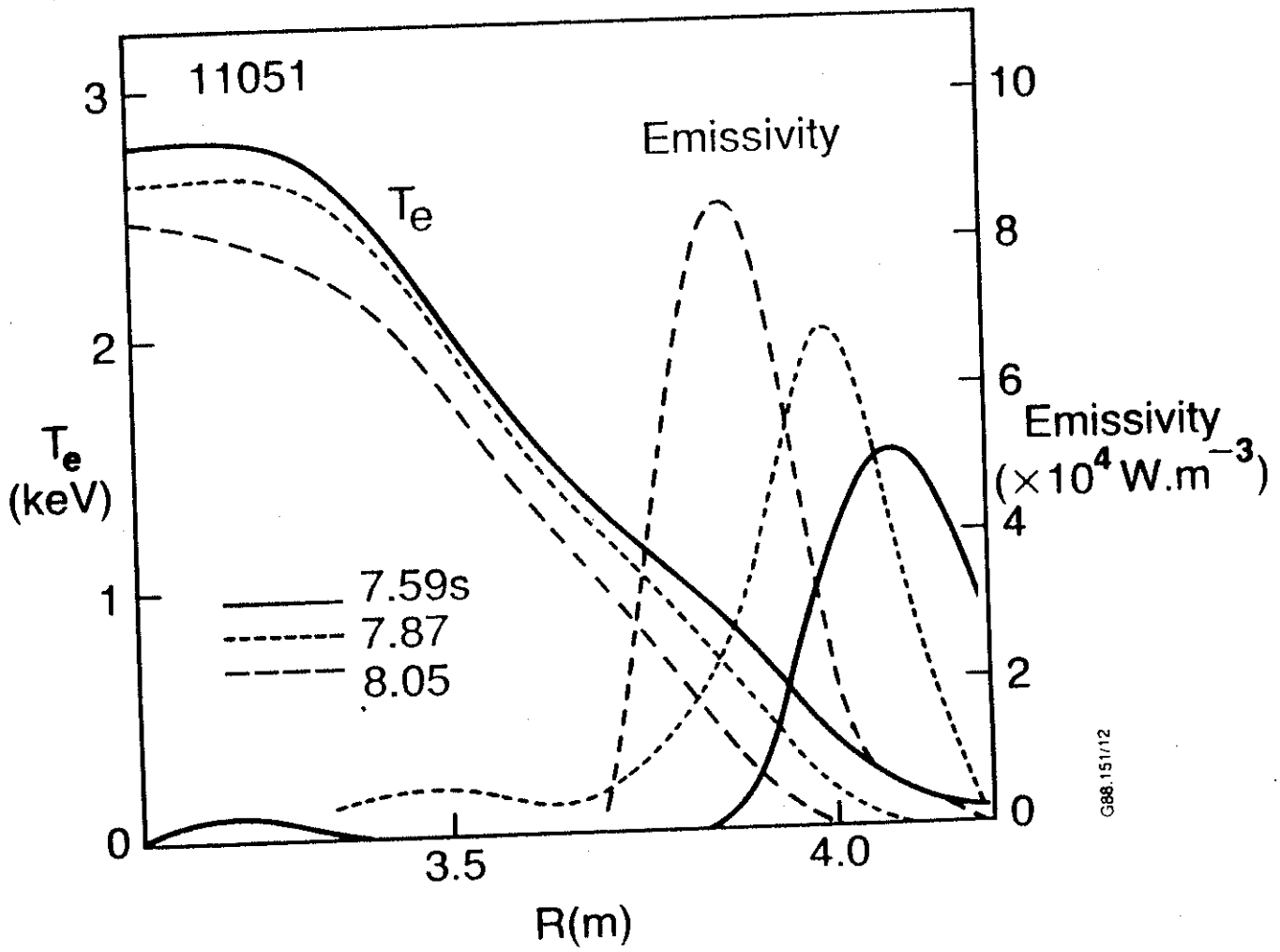

Figure 12 Temperature and radiated power profiles during the plasma contraction

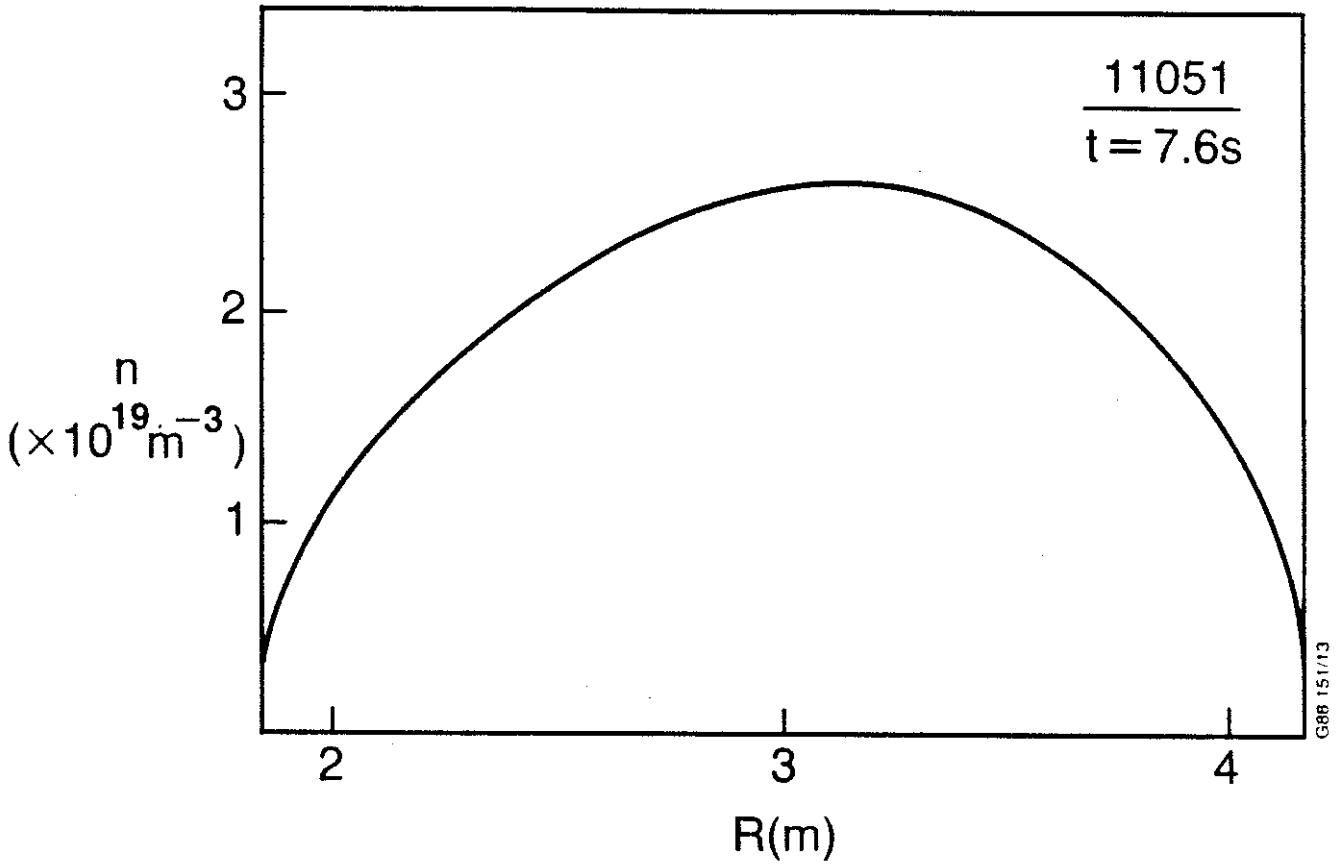

Figure 13 Electron density profile

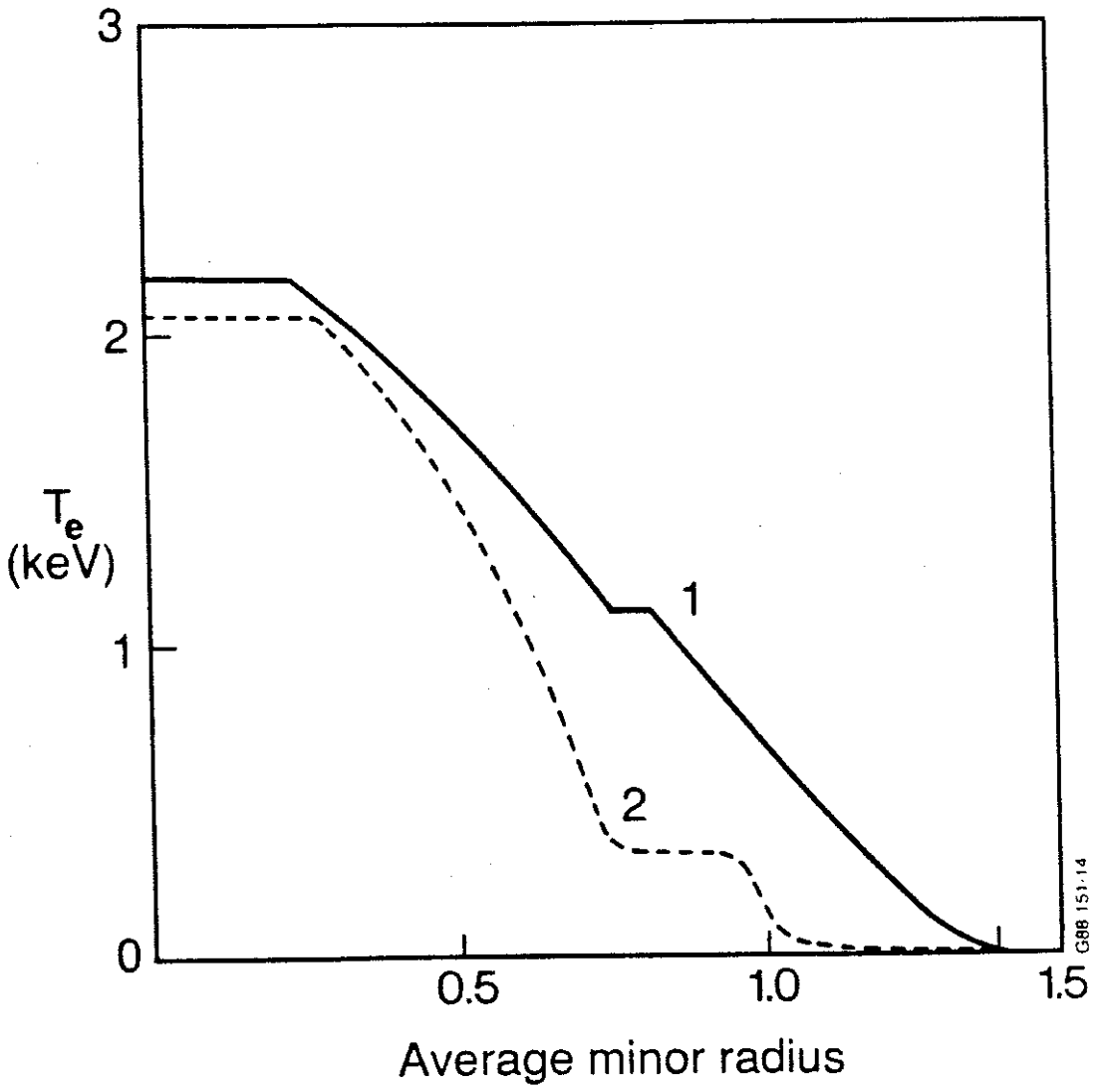

Figure 14 Calculated T_e profiles before (1) and after (2) plasma contraction

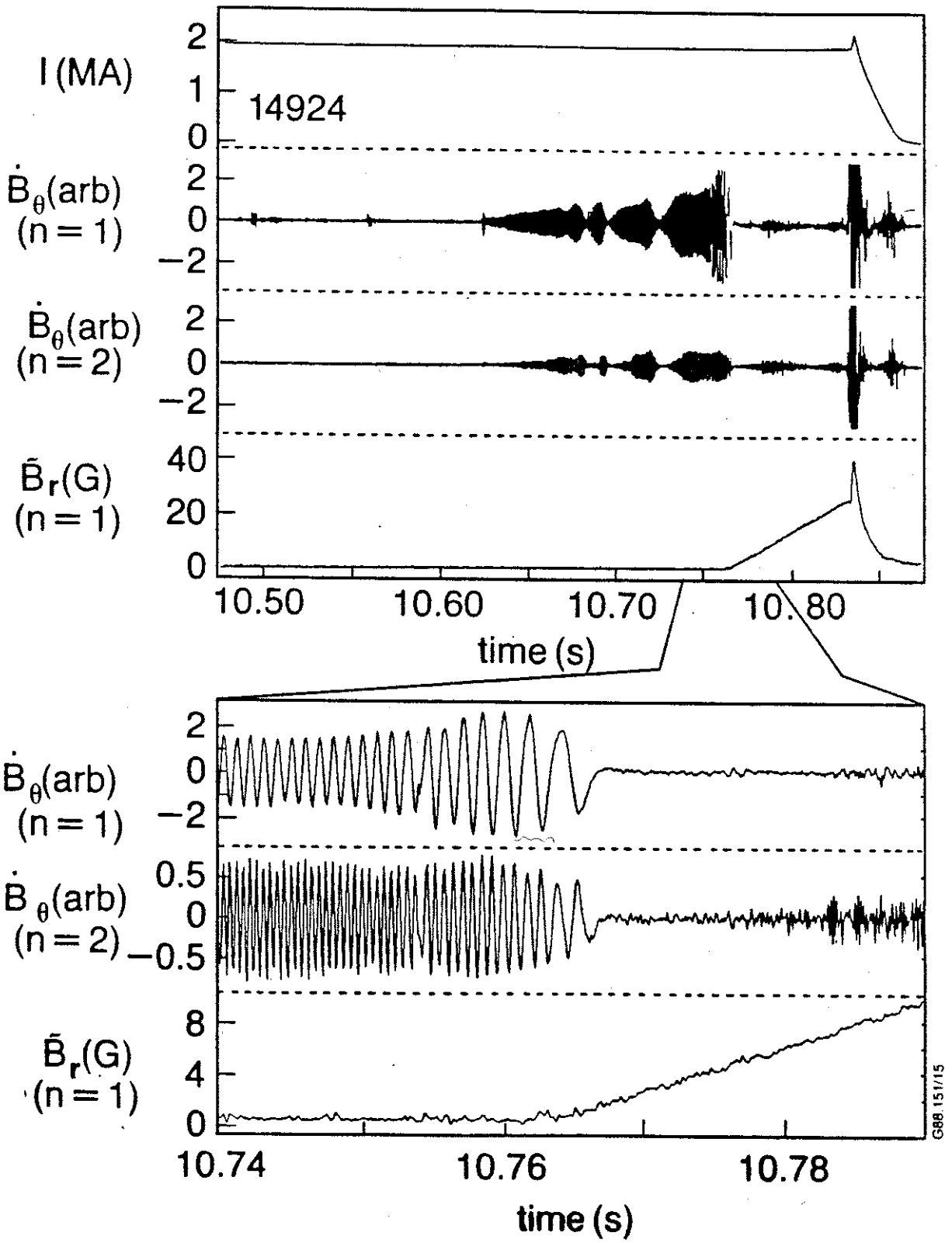

Figure 15 Mode growth and locking before a disruption. The mode locking is shown in detail in the lower part of the figure

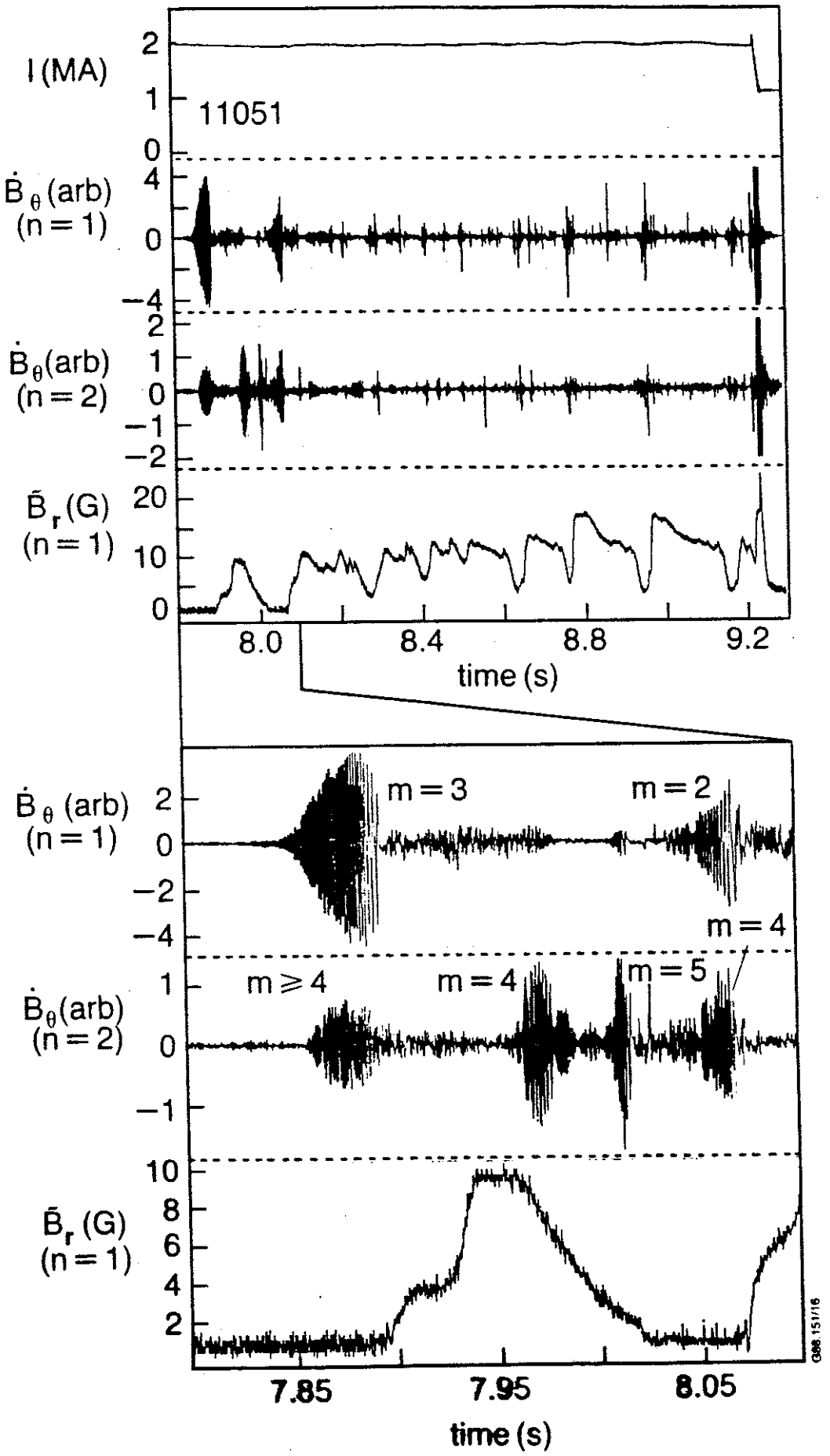

Figure 16 Complex sequence of mhd oscillations and minor disruptions preceding a major disruption at t=9.23s. The m numbers of the mhd oscillations are shown in the expanded lower figure

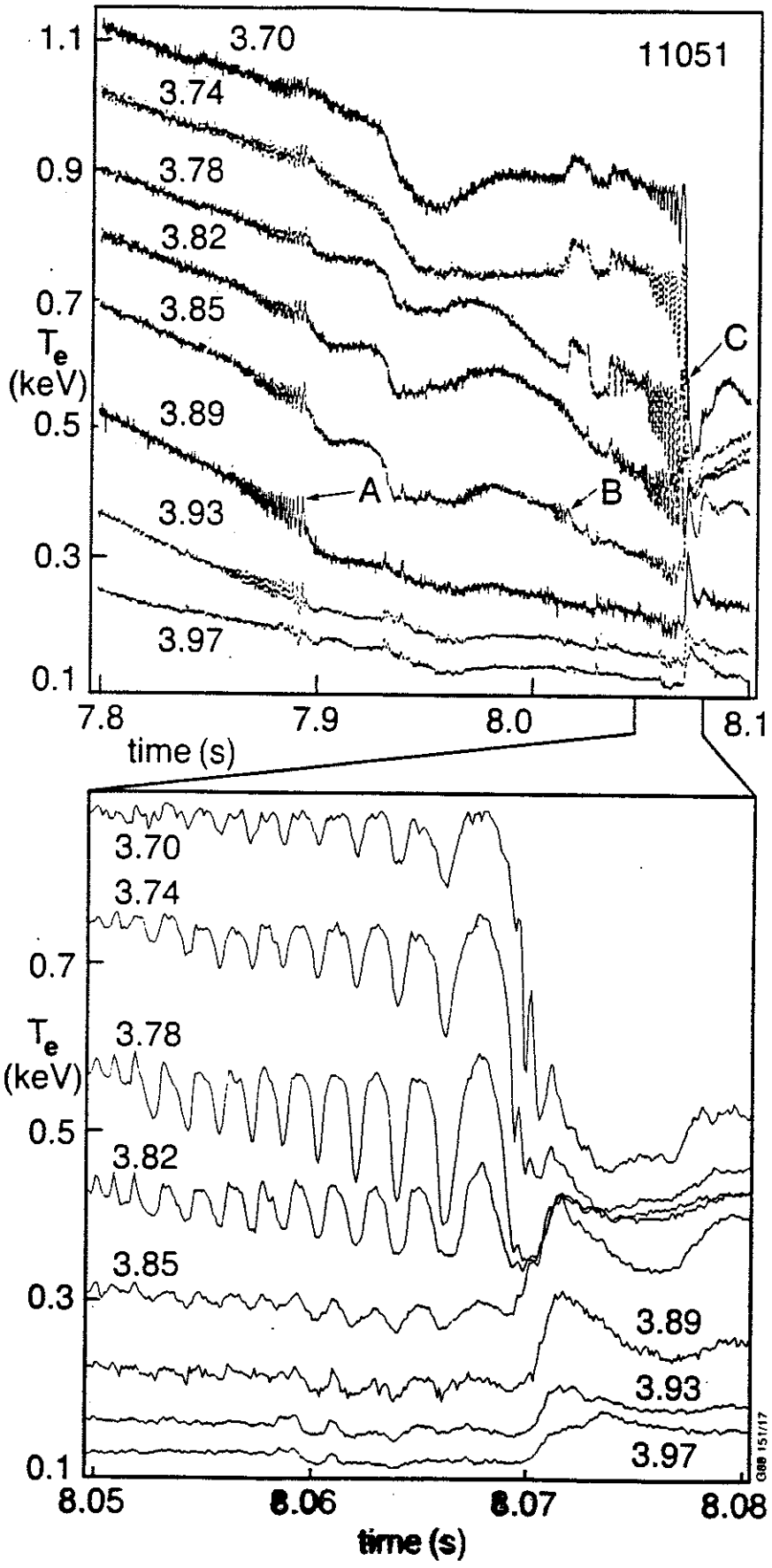

Figure 17 T_e at 8 radial positions. Bursts of mhd activity are seen in the upper figure and the changes in T_e during a minor disruption are seen in the lower figure

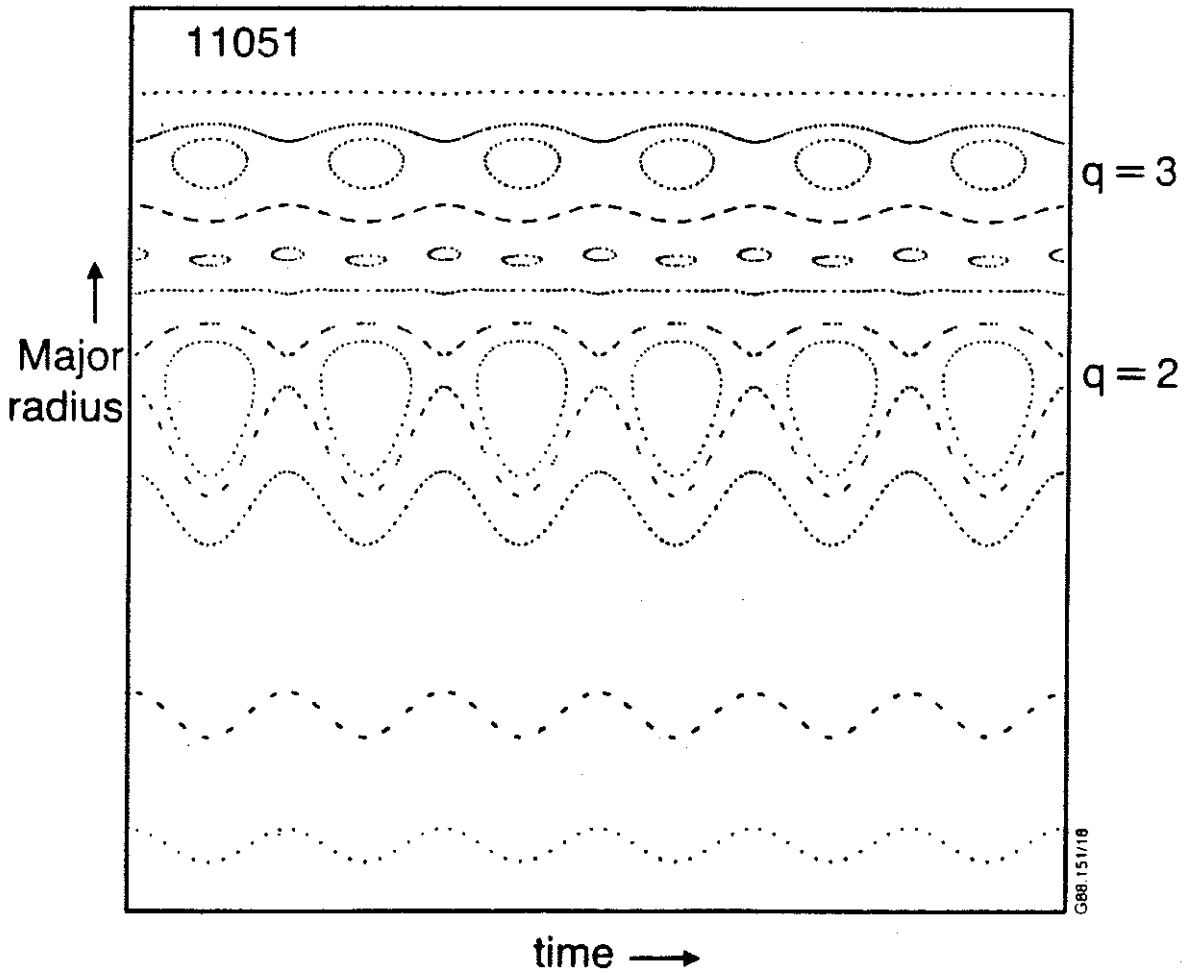

Figure 18 FAR code calculation of magnetic surfaces as a function of time and major radius

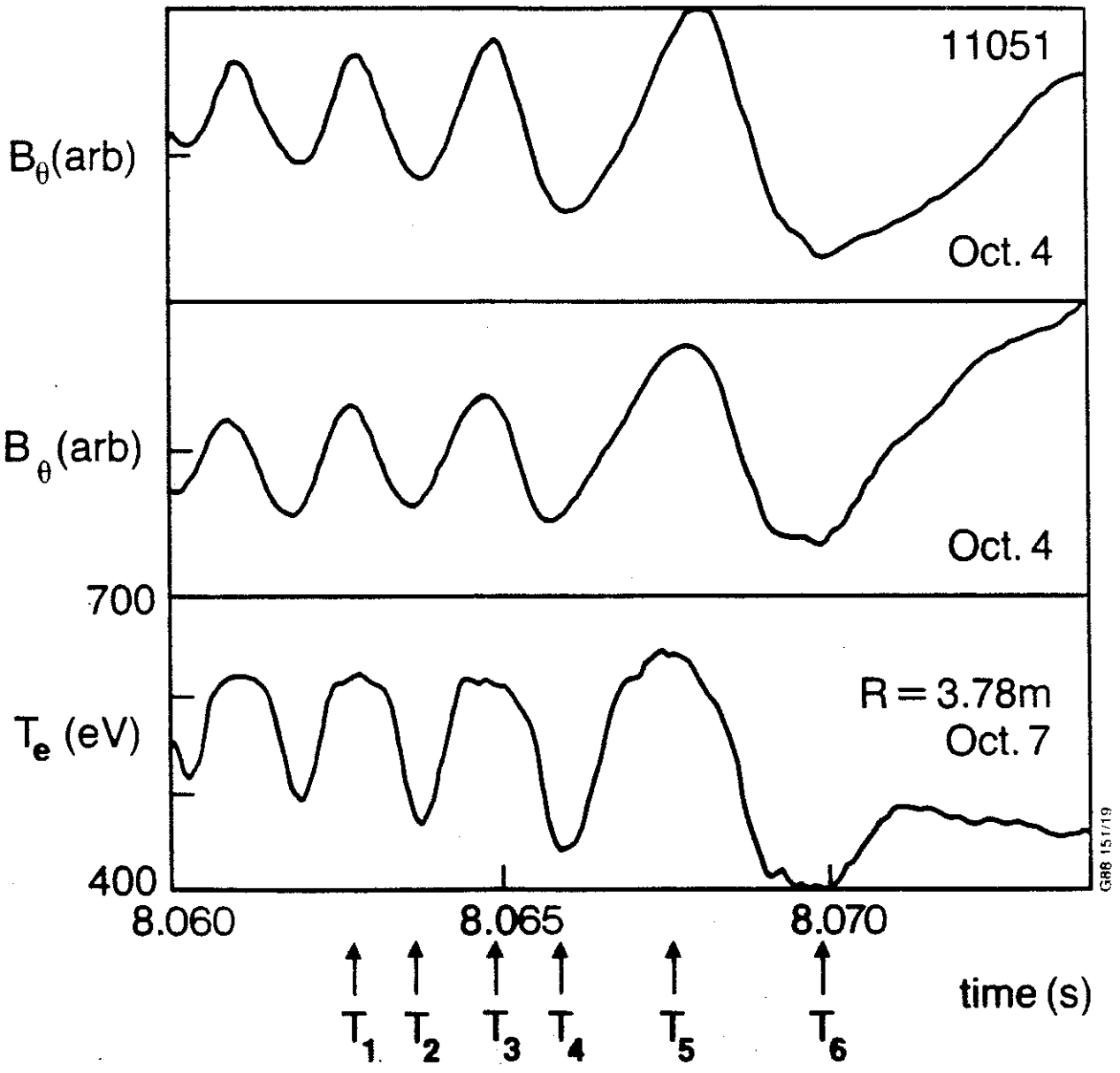

Figure 19 (a) $\tilde{B}_\theta$ and T_e during an m=2 oscillation.

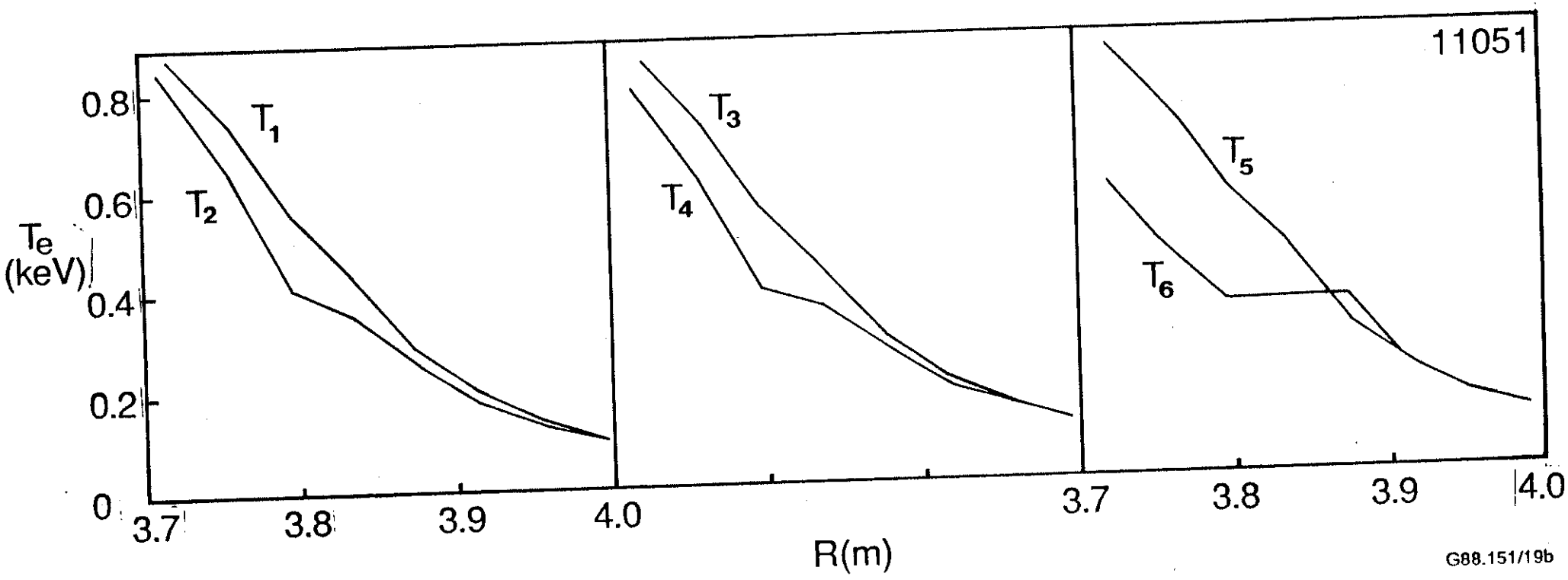

Figure 19 (b) Temperature profiles at the times T_1, T_2 and T_3 indicated in the upper figure show pronounced flattening near q=2

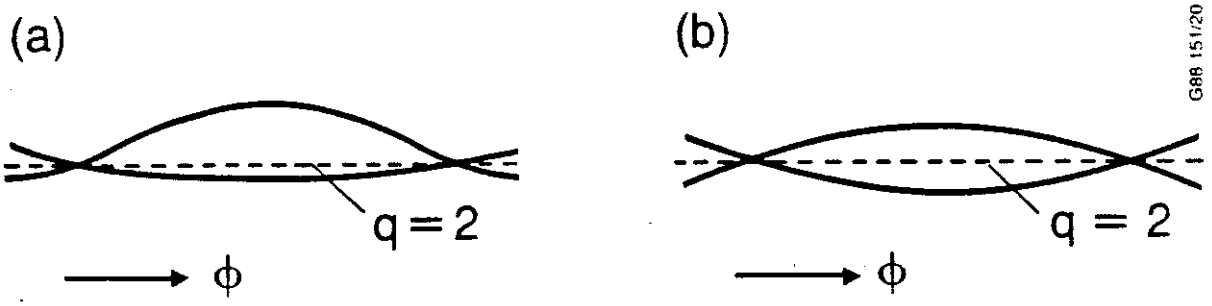

Figure 20 Illustration of the proposed intepretation of the perturbed temperature profile in terms of an asymmetric island (a) as compared with the simple symmetric form (b). (The toroidal coordinate has been straightened for clarity)

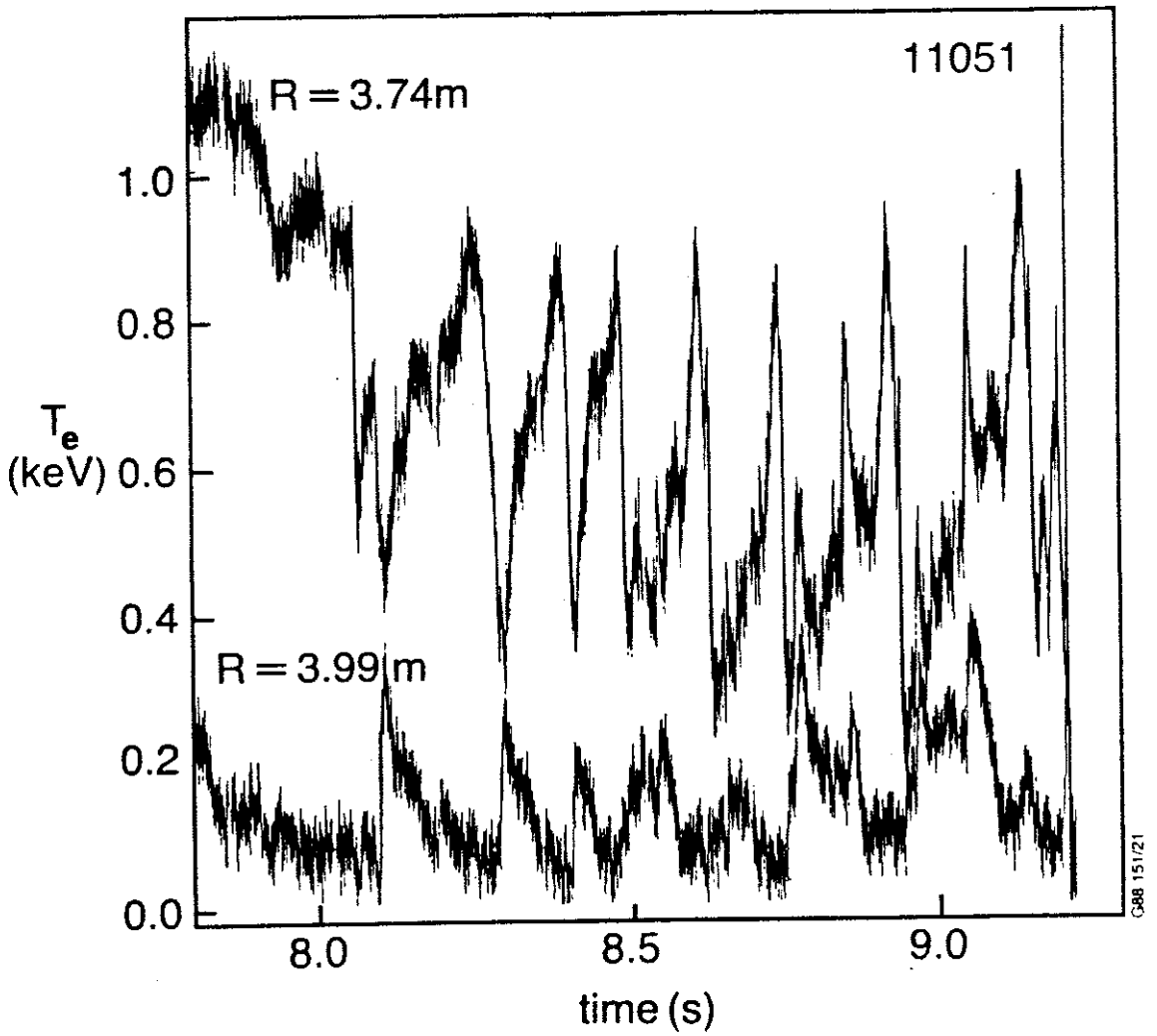

Figure 21 T_e at two radial positions showing the pronounced profile flattening which occurs after minor disruptions. T_e drops inside the q=2 surface (R=3.74m) and increases outside (R=3.99m)

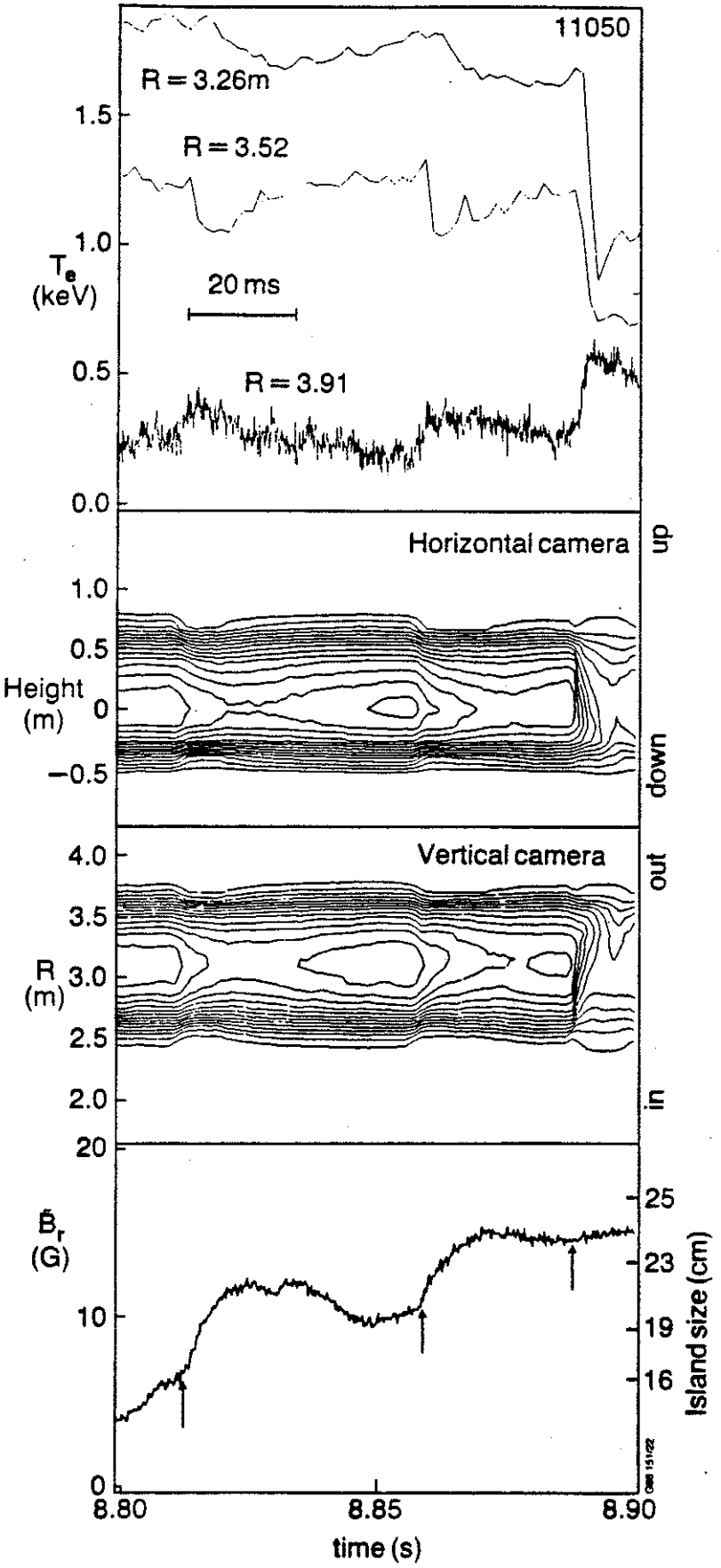

Figure 22 Sequence of three minor disruptions as seen by the ECE (upper) soft X-rays (centre) and magnetics (lower). The last minor disruption has a pronounced asymmetry and little change in $\tilde{B}_r$

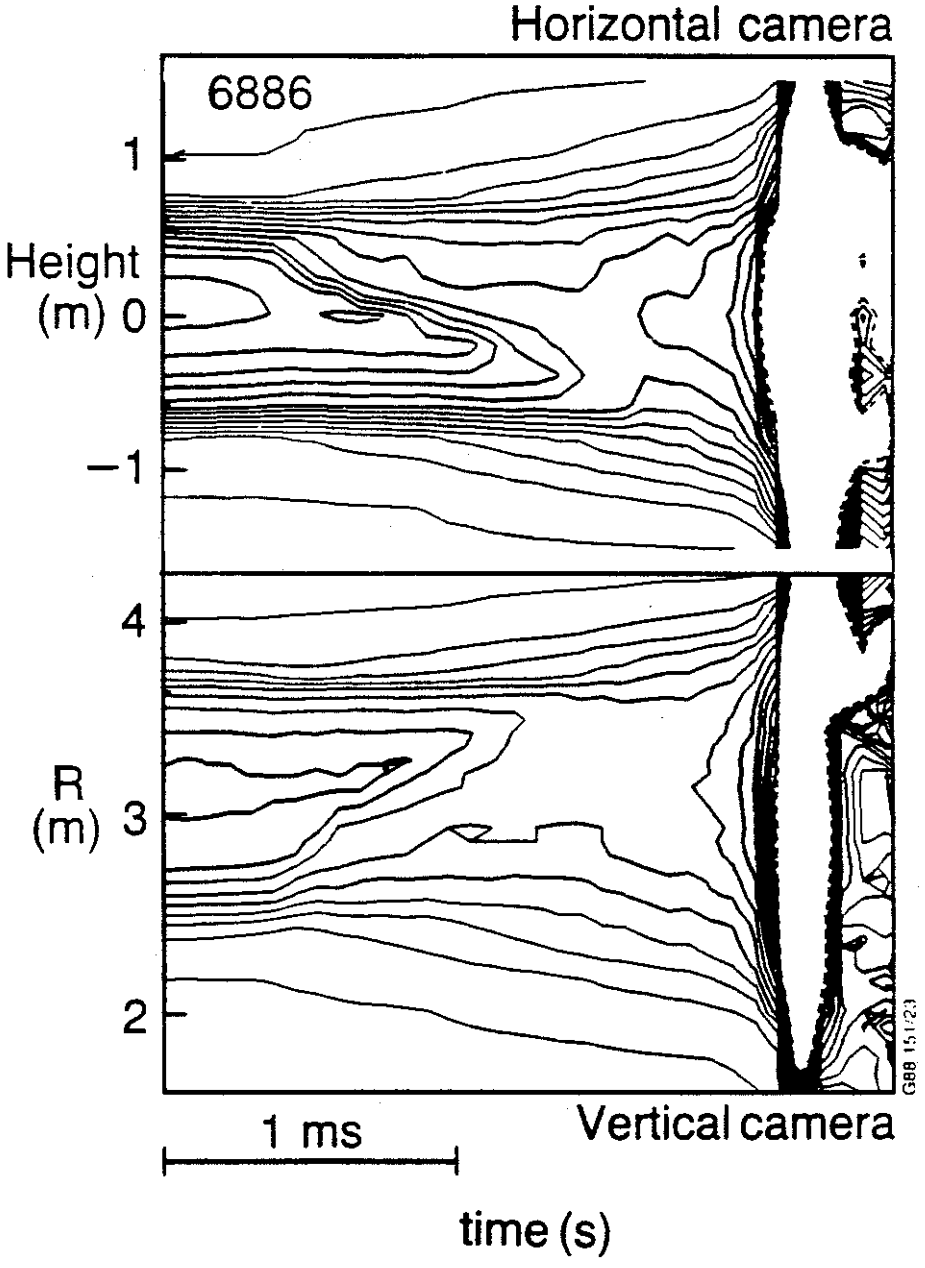

Figure 23 Contour plot of X-ray camera signals versus position and time just before the major disruption. The fast spike at the end is above the highest contour

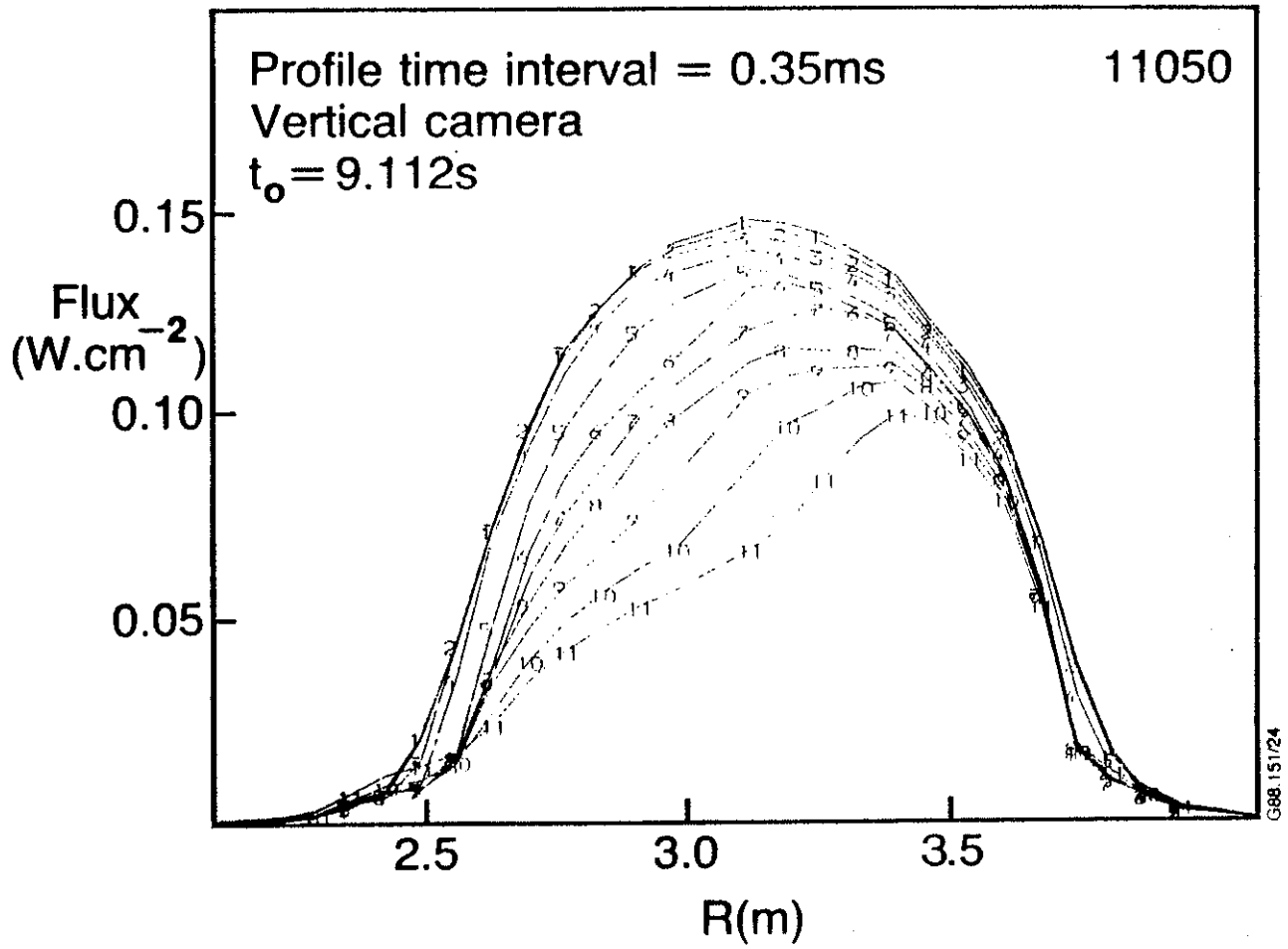

Figure 24 Radial profiles of X-ray signals showing the profile erosion over a time interval of 0.35ms. The profiles 1-11 are aat uniform time intervals

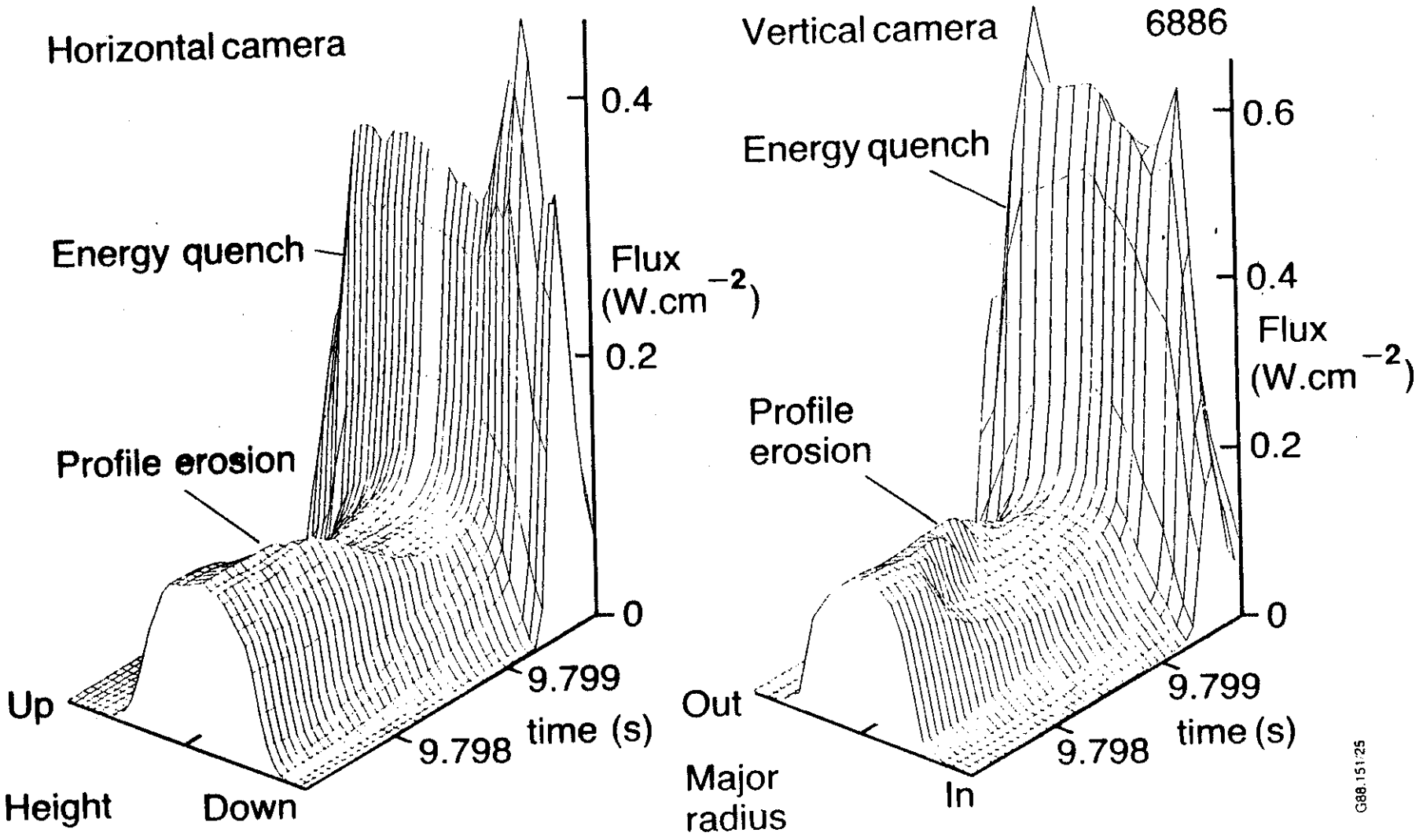

Figure 25 X-ray signals as a function of position and time. The final spike associated with the energy quench is clearly seen

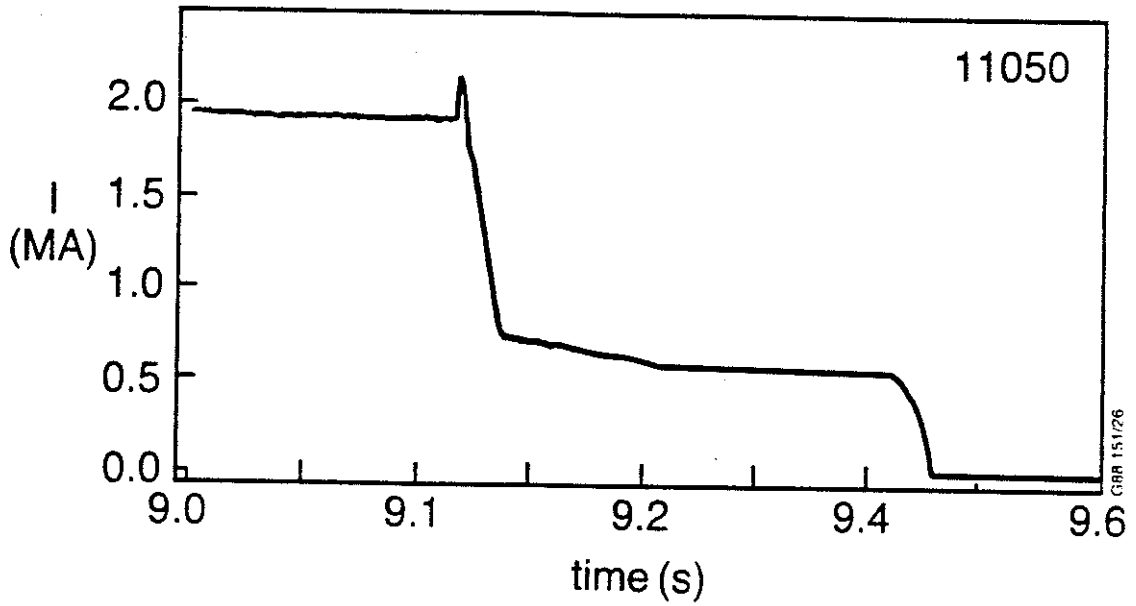

Figure 26 Decay of plasma current following a major disruption. A plateau forms after the first reduction in current

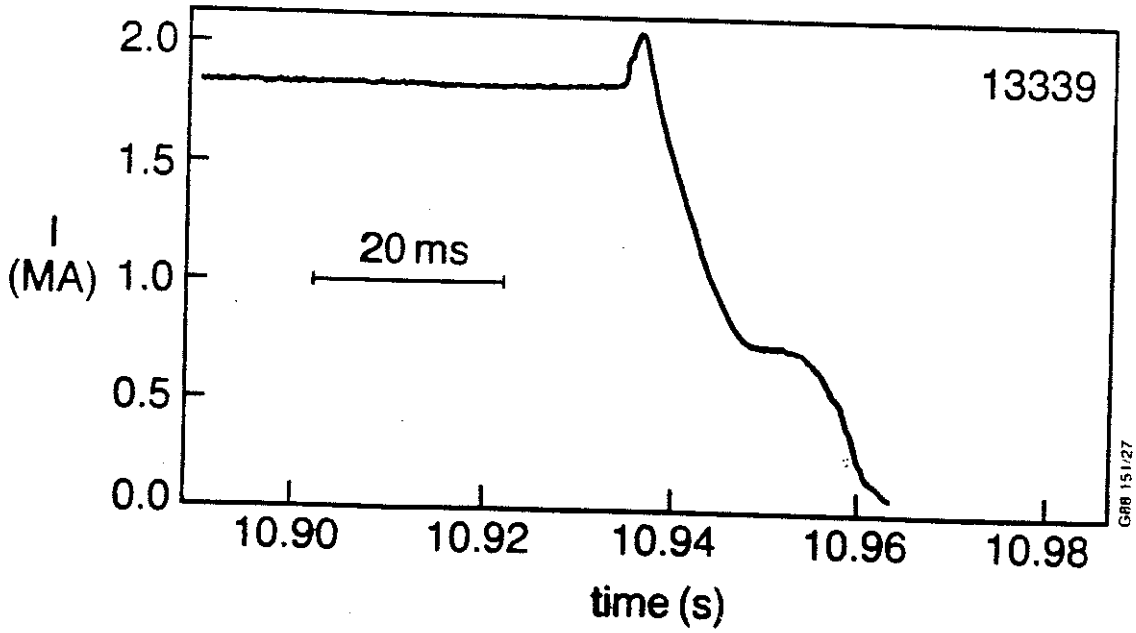

Figure 27 Plasma current trace following a major disruption

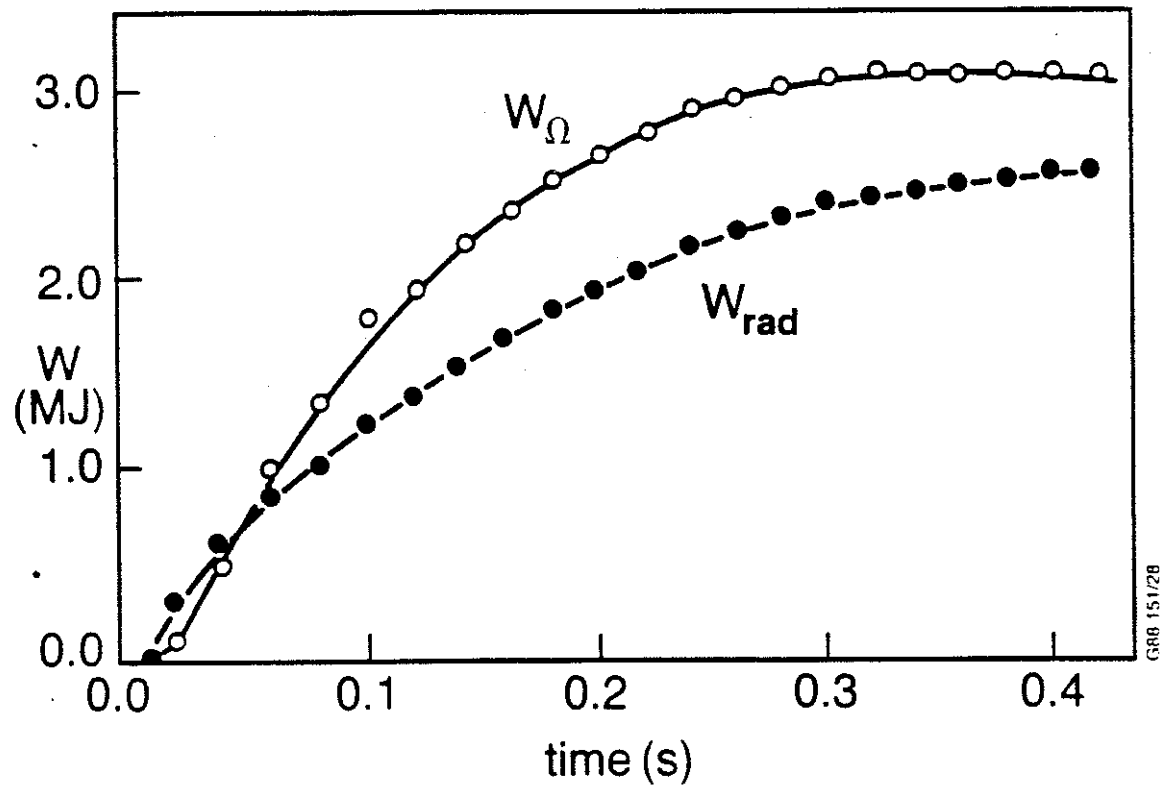

Figure 28 Time dependence of the integrated ohmic power (W_Ω) and radiated power (W_{rad}) following a disruption

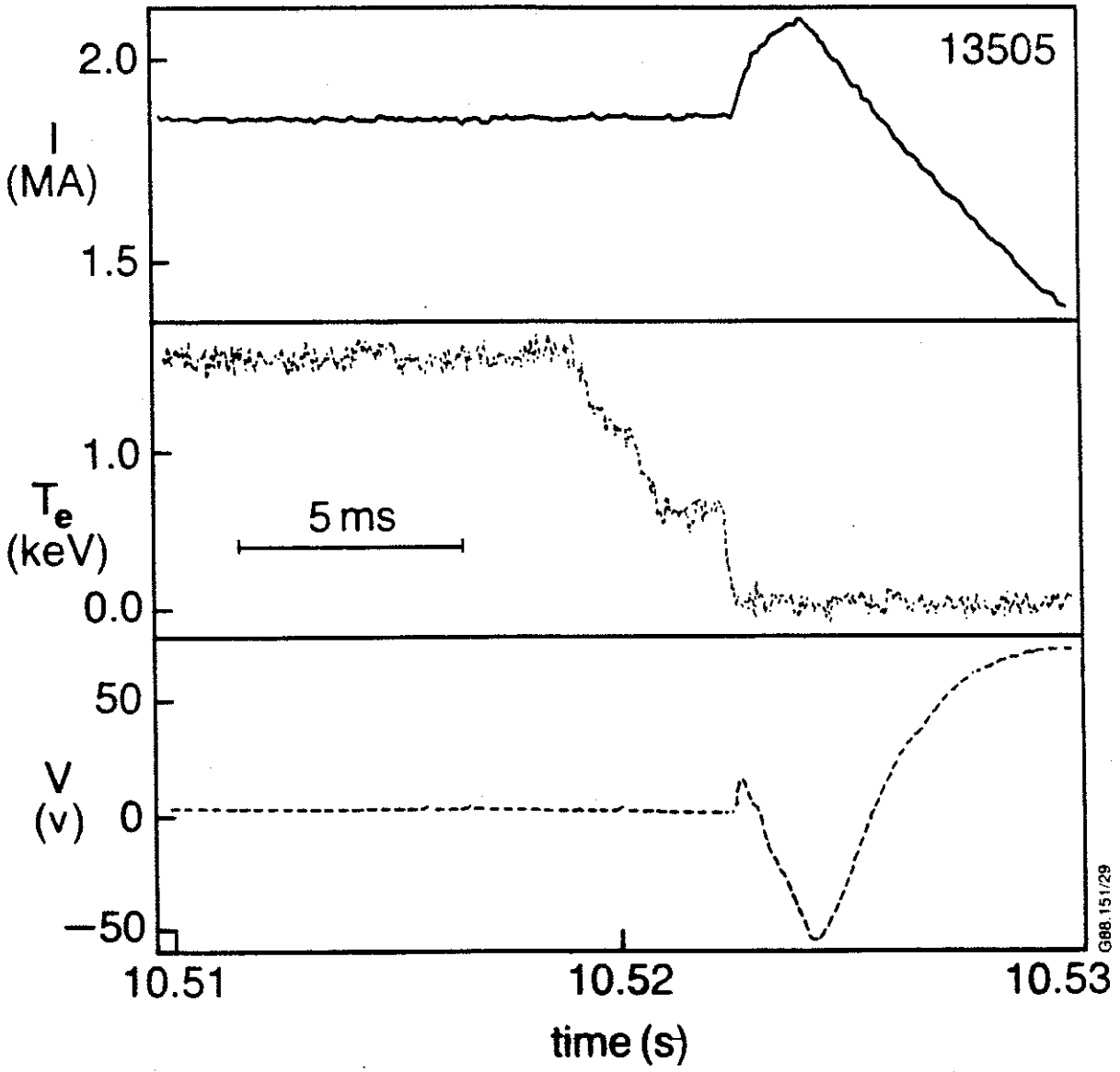

Figure 29 The current increase, temperature drop and negative voltage spike are shown during a major disruption

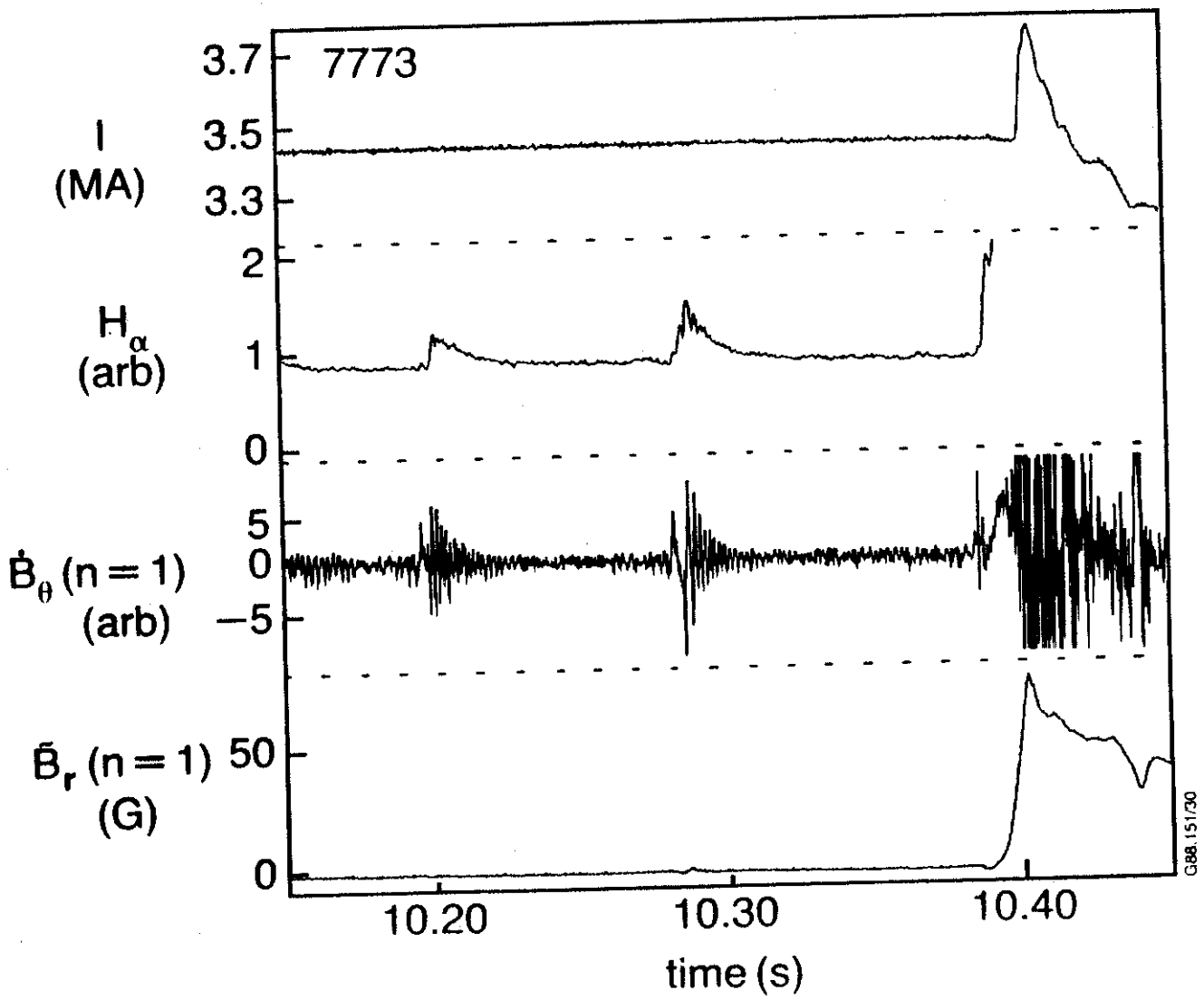

Figure 30 Behaviour of plasma current, H_α, $\dot{B}_\theta$ (n=1) and $\tilde{B}_r$ (n=1) before a major disruption at low q. Sawteeth are present at t=10.2 and 10.3s

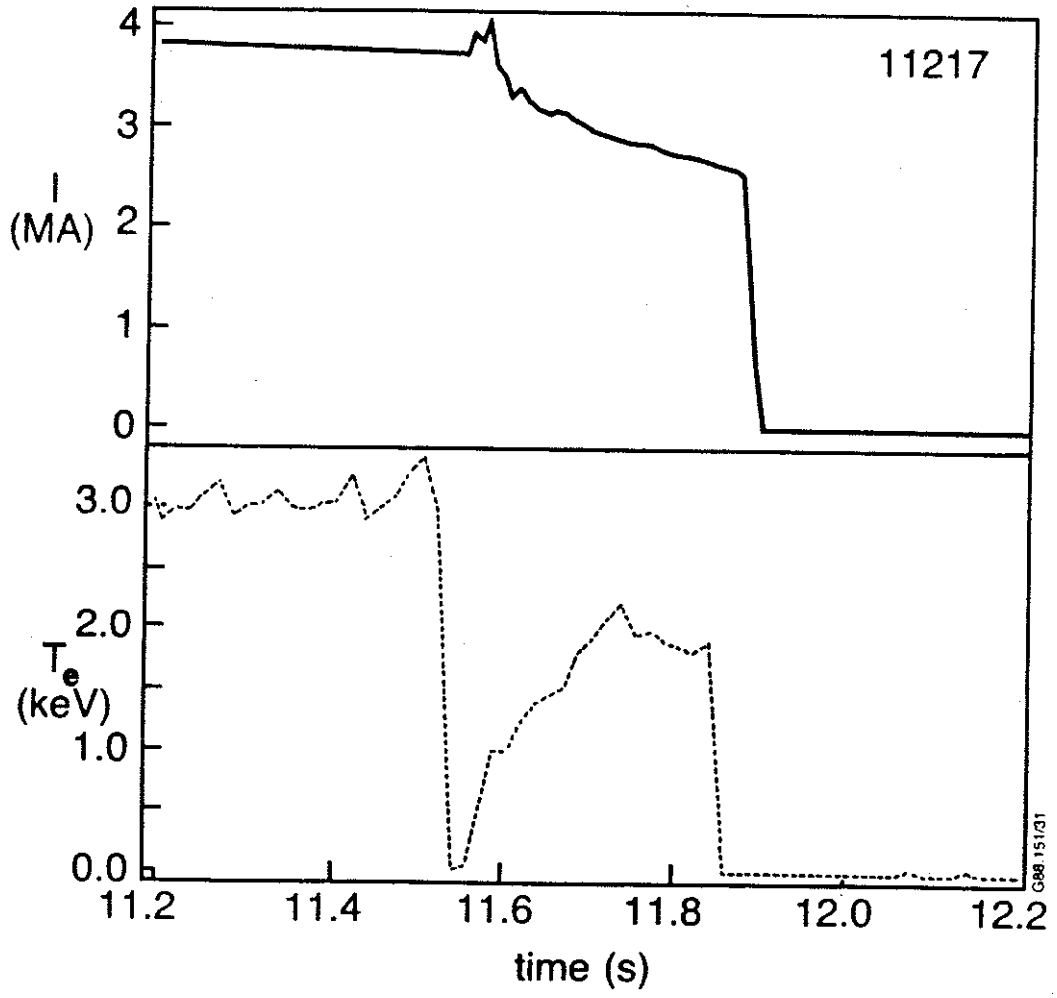

Figure 31 Current decay following a low q disruption. After an initial rapid decay the central temperature recovers and the current decay shows. The discharge is finally terminated by a second disruption

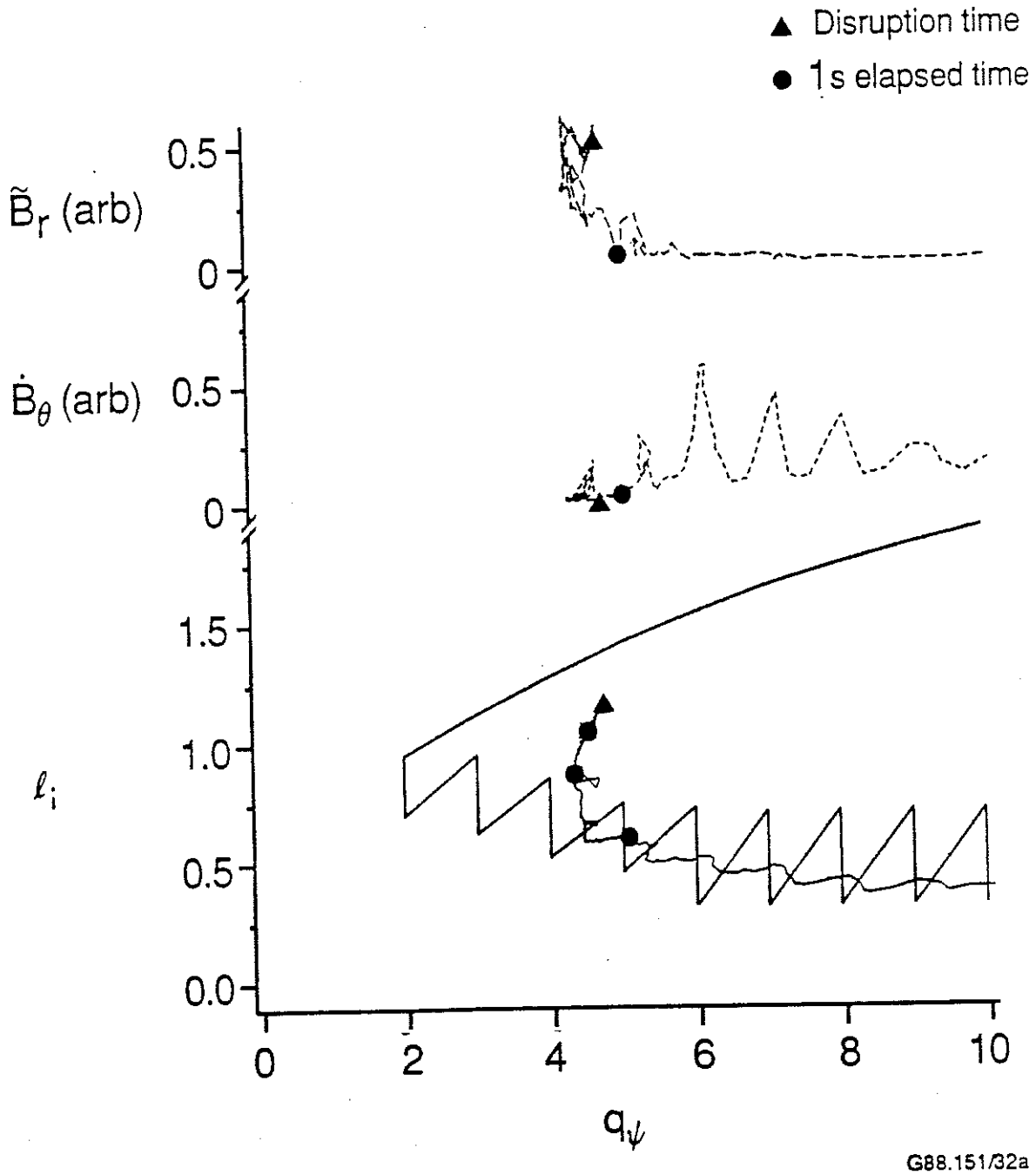

Figure 32 The empirical stability diagram showing the trajectory of a pulse with current rise phase disruptions. The amplitude of rotating and quasi-stationary modes are also shown as functions of edge q_ψ. The symbols indicate 1 s time intervals and the disruption time.

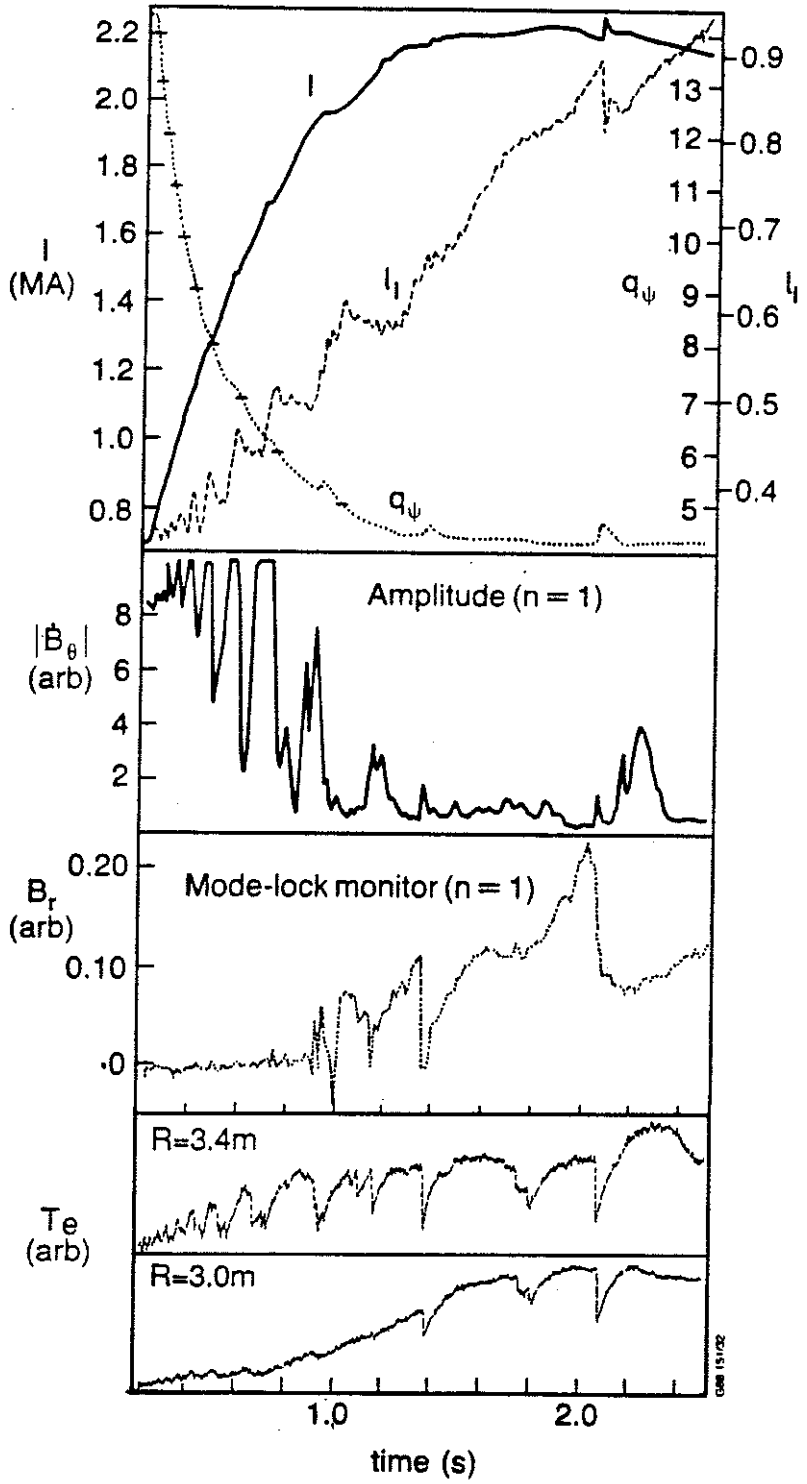

Figure 33 Time behaviour of various signals for a pulse with current rise phase disruptions. The electron temperature data shown correspond approximately to major radii of 3.0 m (axis) and 3.4 m. These temperatures are not absolutely calibrated.

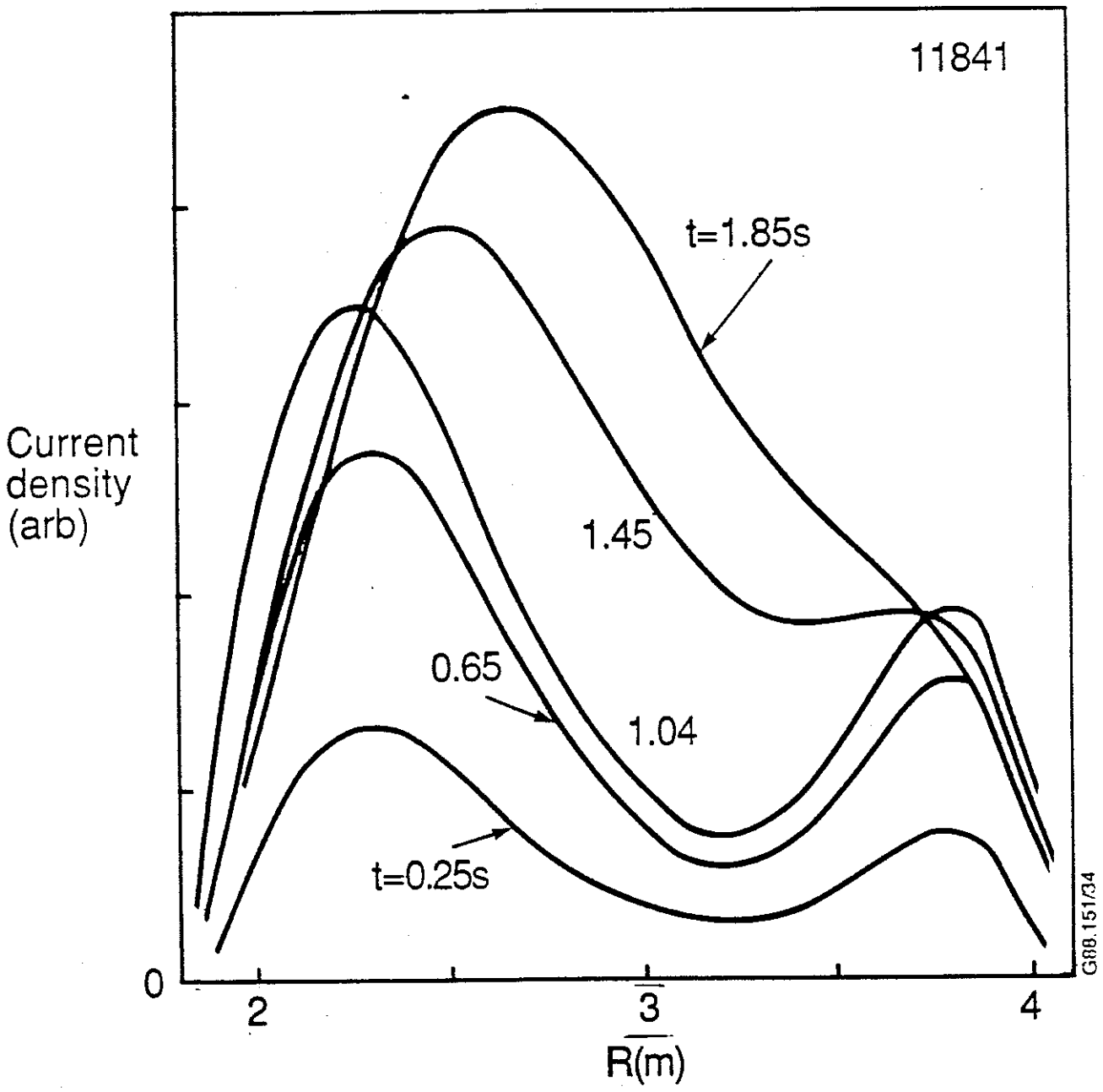

Figure 34 Current profiles during the current rise phase of pulse 11841 at 400 ms intervals. The times are labelled on the curves.

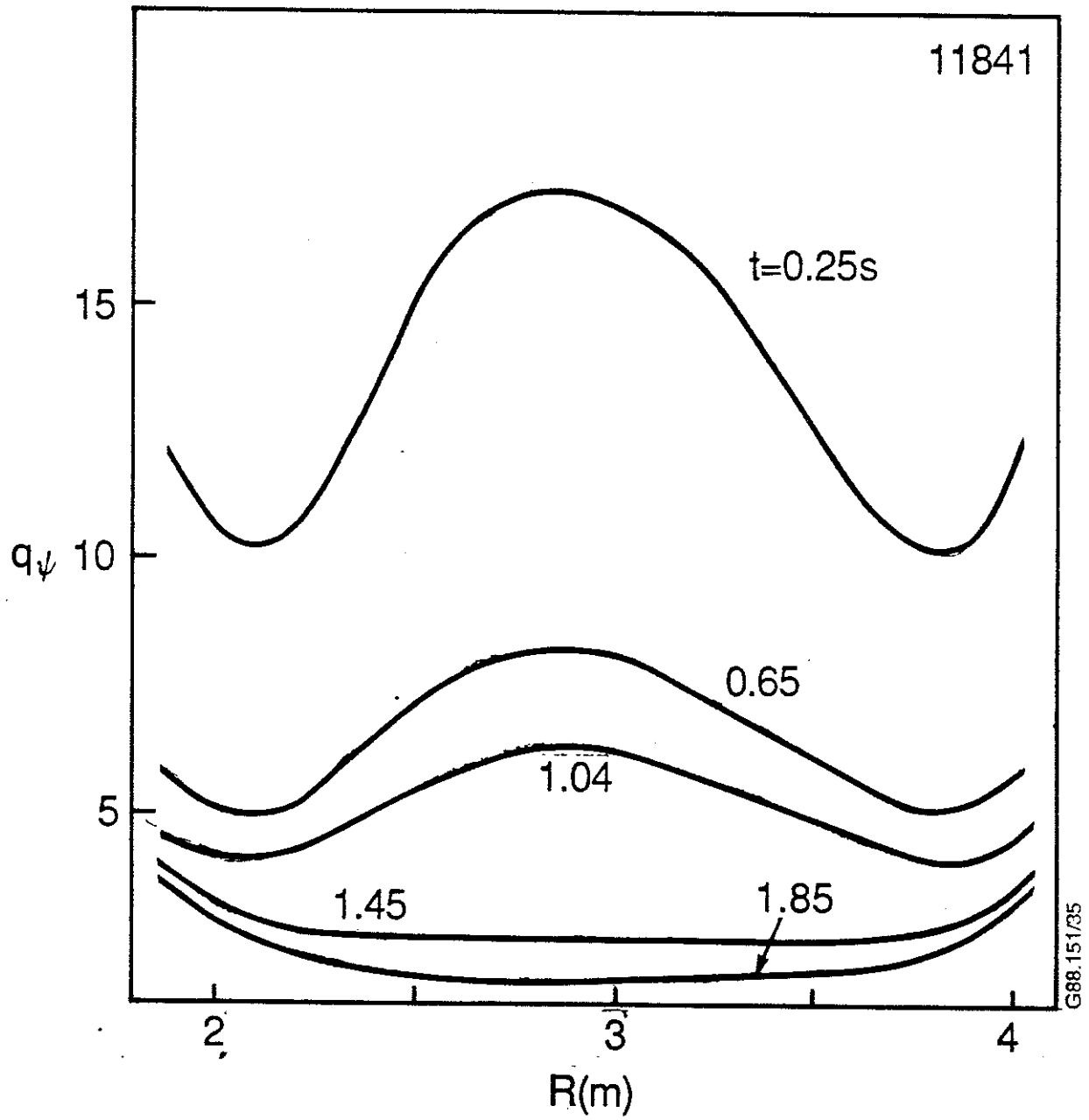

Figure 35 q profiles during the current rise phase of pulse 11841 at 400 ms intervals. The times are labelled on the curves.